CHALMERS
UNIVERSITY OF TECHNOLOGY

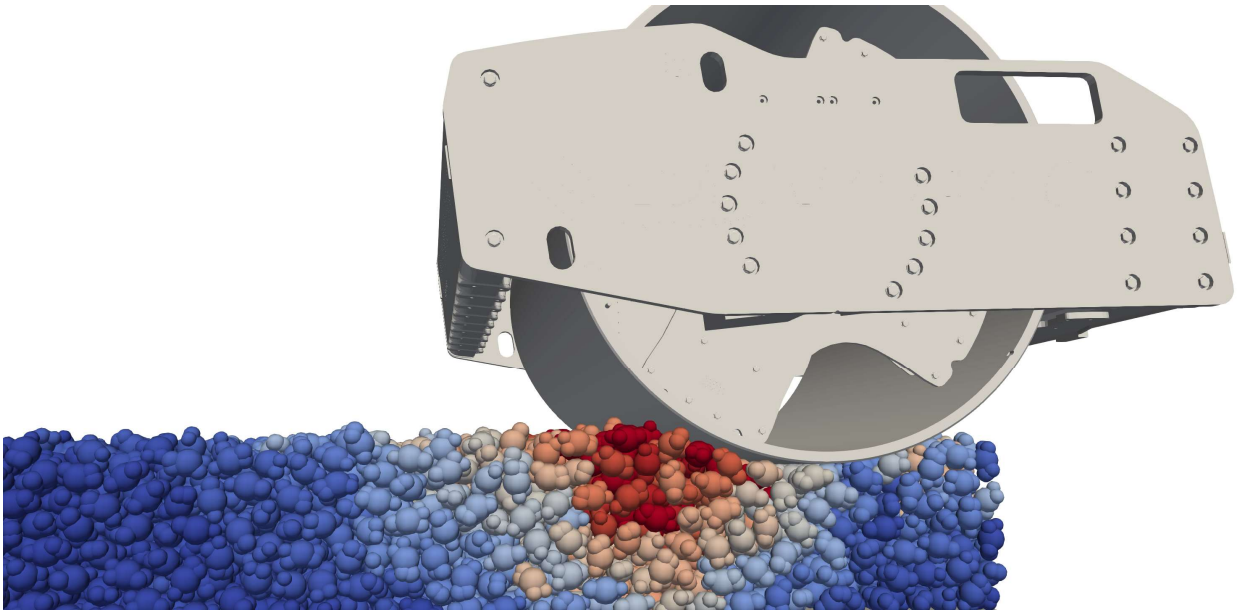

A coupled multibody and discrete element approach for roller compaction dynamics

Master's thesis in Applied mechanics

JOAR GÖRANSSON AXÅS

DEPARTMENT OF MECHANICS AND MARITIME SCIENCES
DIVISION OF VEHICLE ENGINEERING AND AUTONOMOUS SYSTEMS

CHALMERS UNIVERSITY OF TECHNOLOGY
Gothenburg, Sweden 2020
www.chalmers.se

MASTER'S THESIS IN APPLIED MECHANICS

A Coupled Multibody and Discrete Element Approach for Roller Compaction Dynamics

JOAR GÖRANSSON AXÅS

Department of Mechanics and Maritime Sciences
Division of Vehicle Engineering and Autonomous Systems
CHALMERS UNIVERSITY OF TECHNOLOGY

Göteborg, Sweden 2020

A Coupled Multibody and Discrete Element Approach for Roller Compaction Dynamics
JOAR GÖRANSSON AXÅS

Master's thesis 2020:19
Department of Mechanics and Maritime Sciences
Division of Vehicle Engineering and Autonomous Systems
Chalmers University of Technology
SE-412 96 Göteborg
Sweden
Telephone: +46 (0)31-772 1000

Cover:
Compaction simulation of a monodisperse 90 mm particle bed.

Chalmers Reproservice
Göteborg, Sweden 2020

A Coupled Multibody and Discrete Element Approach for Roller Compaction Dynamics
Master's thesis in Applied mechanics
JOAR GÖRANSSON AXÅS
Department of Mechanics and Maritime Sciences
Division of Vehicle Engineering and Autonomous Systems
Chalmers University of Technology

Abstract

This thesis presents a novel compaction simulation method, where a multibody dynamics model of a vibratory roller is coupled to the discrete element method (DEM) for unbound granular materials. A multibody dynamics solver is developed, and an analysis of the roller mechanical system is performed to construct a rigid body model of the machine. Further, a method for bed initialisation is developed, and a uniaxial strain test is used to calibrate the multisphere DEM material parameters. Then, compaction simulation is made possible by implementation of a coupling server, that runs the DEM and multibody solvers simultaneously at different timesteps. Such simulations are compared to full-scale experiments and compaction theory. The machine response to beds of varying stiffness agrees with experience from compaction practice, and characteristic behaviour, such as double jumps, is observed. The stresses in the bed agree with experiments if the particle Young's modulus is kept low. However, the roller penetration of the bed is higher than in experiments due to insufficient shear resistance in the DEM model. At the same time, no increase in bulk density is achieved. Further analysis shows that the lack of shear resistance is likely related to the multisphere model of the particle geometry, and the lack of compaction may be due to a particle size distribution that is too narrow. On the other hand, such simplifications are necessary, because large computational costs impose limits on the particle size distribution, particle discretisation, and domain size. The function of the solver coupling and machine model is verified, but in order to enhance agreement with full-scale experiments, improvements are needed in terms of both the particle modelling and computational performance capacity.

Keywords: Compaction, discrete element method, multibody dynamics, vibratory roller, model coupling

Preface

In this work, vibratory roller compaction is simulated by combining a discrete element model of the compacted material with a multibody dynamics model of the machine. The thesis is carried out at the Fraunhofer-Chalmers Centre for Industrial Mathematics in Gothenburg from January to May 2020. The project is carried out with Dr. Johannes Quist as supervisor and Dr. Klas Jareteg as co-supervisor. The examiner is Associate Professor Mathias Lidberg.

This thesis is carried out within the scope of the Vinnova InfraSweden2030 project Digiroad. Vinnova InfraSweden2030 is a national strategic innovation program in infrastructure. The Fraunhofer-Chalmers Centre coordinates the project (2018-00606 DigiRoad Simulation of handling and compaction of unbound aggregates in road construction) within the program which focuses on developing a virtual development environment for unbound granular materials in roads. Swedish roller compactor manufacturer Dynapac AB is another stakeholder in the Digiroad project.

I would like to thank my supervisor, Dr. Johannes Quist, for enlightening discussions, insight into rock mechanics, and an unforgettable research trip to Karlskrona. Thank you also to Dr. Klas Jareteg, for your patience and assistance with all things related to DEM.

A warm thank you to Andreas Persson and Michael Knutsson at Dynapac, for assistance with data and information on the machine, as well as the hands-on experience of roller compaction.

The simulations were performed on resources at Chalmers Centre for Computational Science and Engineering (C3SE) provided by the Swedish National Infrastructure for Computing (SNIC).

Gothenburg May 2020

JOAR GÖRANSSON AXÅS

Contents

Abstract i

Preface iii

Contents v

1 Introduction 1
1.1 Objectives . . . 1
1.2 Delimitations . . . 2
1.3 Layout of the thesis . . . 2

2 Roller Compaction 5
2.1 Drum-ground interaction . . . 5
2.2 Ground stiffness estimation . . . 6
2.3 Prevalent simulation methods . . . 7
2.3.1 Spring-damper ground models . . . 8
2.3.2 FEM ground models . . . 8
2.3.3 DEM ground models . . . 8
2.3.4 DEM-MBS coupling . . . 9
2.4 Coupling methods for compaction simulation . . . 9

3 Multibody Roller Modelling 11
3.1 Constrained rigid body dynamics . . . 11
3.1.1 Newton-Euler equations . . . 11
3.1.2 Quaternions . . . 12
3.1.3 Equation system with constraints . . . 13
3.1.4 State vector transformation . . . 16
3.2 Machine specifications . . . 16
3.3 Modelling assumptions . . . 16

4 Particle Bed Modelling 21
4.1 Discrete element method . . . 21
4.1.1 Contact force . . . 21
4.2 Multisphere model and size distribution . . . 22
4.3 Bed generation method . . . 24

5 Coupling of the Multibody Solver to DEM 27
5.1 System solution and algorithm . . . 27
5.2 Verification of the roller model . . . 27
5.3 Model coupling theory . . . 29
5.4 Implementation of a coupling server . . . 30
5.5 Verification of the coupled model . . . 31

6 DEM Calibration and Compaction Experiments 33
6.1 Calibration of DEM material parameters . . . 33
6.1.1 Previous work on calibration for compaction . . . 33
6.1.2 Uniaxial strain test . . . 33
6.2 Compaction experiments setup . . . 36

7 Compaction Simulation Results **39**
7.1 Simulation assumptions 39
7.2 Bed displacement profile 40
7.3 Load cell response 41
7.4 Drum response to impact 43
7.5 Discussion of results and model limitations 45

8 Conclusions **47**

References **49**

1 Introduction

Ground compaction is essential in road construction. Compaction increases the stiffness of the road layers by reducing the amount of air in voids and increasing the number of contact points between particles, which substantially improves road durability and stability [1, 2]. The compaction is performed with a vibratory roller, which is composed of a driving rear unit with off-road capabilities linked to a vibrating drum as a front unit. The drum is excited by a built-in rotating eccentric shaft, and the road material is compacted by the impact and kneading effect of vibrations.

Roads consist of several layers: the subgrade, subbase, base course, and surface course. The native material under the road is known as the subgrade, often consisting of soil. The subbase rests on top of the subgrade, and its role is to evenly distribute the loads over the ground. The layer above the subbase is referred to as the base layer or base course. The subbase and base course can consist of unbound granular materials (UGMs), or a cement-bound aggregate. The surface course is the layer in contact with traffic, usually consisting of hot mixture asphalt [3]. This work focuses on simulation of the UGMs in the subbase and base layer.

Each of the road layers, from the subgrade to the surface course, must be compacted until a bulk stiffness prescribed by regulations is reached (e.g. [4]). A standardised number of roller passages is performed over each layer. Still, studies show that additional compaction of UGMs beyond the legal requirements may result in a significant increase in road lifetime and quality [5]. Therefore, a balance must be struck between the cost of increasing the number of passages and the compaction on the one hand, and the gain in longevity and saved maintenance costs for society over the road lifetime on the other. However, solution of this problem requires understanding of the complex compaction process.

The compaction performance is influenced by several factors, including machine vibratory settings, weight and size of the roller, water content, the material and density of the compacted particles, as well as the characteristics of the subgrade [2]. Variations in the ground properties can therefore lead to an uneven compaction performance. As a solution, on modern vibratory rollers operational parameters are adjusted continuously from machine feedback, which is referred to as Intelligent compaction [6, 7]. This has motivated a large body of research on how to properly model ground-roller interaction to enable prediction of how machine parameters affect compaction on different ground types.

Finite element analysis can be used to model the ground deformation in 3D, under the assumption that the particulate material behaves as a continuum in general. Another approach is to use discontinuous models. One such model, originally introduced by Cundall and Strack [8], is the discrete element method (DEM). With DEM, particles are modelled as rigid bodies, and contact forces are implemented with the aim of capturing the bulk behaviour of particulate matter. In this project, the ground is modelled with multisphere clumps whose shapes are based on data from scanned gravel grains.

There is a body of research on compaction simulation with DEM and FEM, as further described in Chapter 2. The drum models used are usually a cylinder in 2D [9, 10, 11, 12] or 3D [13] with a prescribed movement or load. However, the simulation could be enhanced by combination of the particle solver with a multibody dynamics (MBD) model of the roller system of components. A coupled method has the potential to capture a more realistic drum response to the bed impact. This thesis presents the development of such a method. To the author's knowledge, no previous coupled DEM-MBD simulations of compaction have been performed at this level of detail.

The DEM-MBD method is realised by coupling the DEM solver Demify®, developed at Fraunhofer-Chalmers Centre of Industrial Mathematics, to a separate multibody solver (MBS) written within the scope of this project. This multibody solver is a lightweight Python tool that solves rigid body systems with user-defined bodies, constraints, and loads. A coupling server handles the simultaneous operation of two solvers. The contact forces calculated from the overlap of particles and the drum in Demify are continuously added as a load on the drum body in the multibody model. The resulting movements of the machine parts are then calculated and imposed as drum movement in the DEM solver.

1.1 Objectives

The goal of this project is to enable a complete particle-machine co-simulation of roller compaction based on the discrete element method with multisphere particles, and a multibody dynamics model for the roller dynamics. In order to reach this objective, several problems need to be solved. First, a multibody dynamics simulation method of sufficient detail and accuracy must be developed and implemented. Second, a representative

multibody model of a vibratory roller must be designed and implemented. Third, the ground DEM model must be calibrated with regard to material parameters, particle size, and shape discretisation, and representative beds generated. Fourth, a co-simulation framework must be implemented, that manages to simultaneously run the DEM and MBD solvers and handle the transfer of information between them. Finally, correct implementation of all four steps must be verified via simulation of systems with known analytical solutions or comparison to empirical data.

In addition to these objectives, that focus on implementation, development of a coupled DEM-MBD solver enables measurement of several interrelated compaction phenomena. Once implemented, the solution method is also used to measure such phenomena. The objective is to analyse the performance of the method in relation both to roller compaction theory and experiments. In this context, the following research questions are investigated.

- Measurement of UGM particle bed stiffness from simulated compaction, and comparison of stiffness results to prevalent ground-compaction theory.
- Measurement of contact forces on the roller.
- Study of particle size distribution effects on the bed stiffness and compaction quality.
- Study of the dynamical reaction of the roller to ground stiffness, such as lift-off, double jump, and rocking.

1.2 Delimitations

The main limitations of the project are time and computational resources. Therefore, prioritisation is necessary both with regard to the depth of study in the fields covered by the thesis, and in what simulations to run. This motivates the following delimitations.

- The currently available contact force model will be used. No additional models are developed.
- The machine dynamics are formulated for the roller front module, and do not explicitly include the complete machine with the steering hitch and back wheel transmission.
- The purpose of the study of vibrations is on the drum interaction with the material, not on driver comfort or the structural vibrations in the machine.
- Although soil compaction theory will be studied for its general applicability, the main aim is to simulate aggregates and no finer kinds of soil.
- A general rigid body solver is developed, but primarily, only the joints and load types necessary for the roller model are implemented.
- No optimisation of machine parameters for compaction will be performed.

1.3 Layout of the thesis

Each of the chapters 2-6 presents one independent part necessary for a coupled simulation of compaction.

Chapter 2 covers the essential theory on roller compaction. The drum moves differently on soft and stiff particle beds, and consequently, the bed stiffness can be approximated from the drum movement. A background to previous work on compaction simulation and multibody coupling to DEM is also given here, and the relevance of this thesis is further underlined in relation to the literature.

In Chapter 3, the multibody solver is described. The theoretical background to constrained rigid body dynamics and quaternions is given. In addition, the chapter describes the process of extracting the critical mechanical properties of the machine and modelling the front module as a multibody system.

Chapter 4 contains all modelling assumptions related to DEM. First, an introduction to DEM is given, and the contact force is defined. Further, the particle multisphere model is motivated, as well as the particle size distribution. Finally, the bed initialisation is covered.

In Chapter 5, the algorithm for the multibody solver is described, and a theoretical background to DEM-multibody co-simulation is given. The co-simulation methods used in this work are described and motivated, and verification of the coupled solver is performed.

Chapter 6 contains a section on calibration of DEM material parameters. The chapter also outlines the experiments performed within "WP4 - Full-scale experiments" of Digiroad. A subset of results of interest to this thesis are presented [14].

The results of these chapters are then synthesised in Chapter 7, which covers the main simulation results. The coupled model is applied to simulate compaction, and the results are compared to compaction theory and experiments. Finally, conclusions are summarised in Chapter 8.

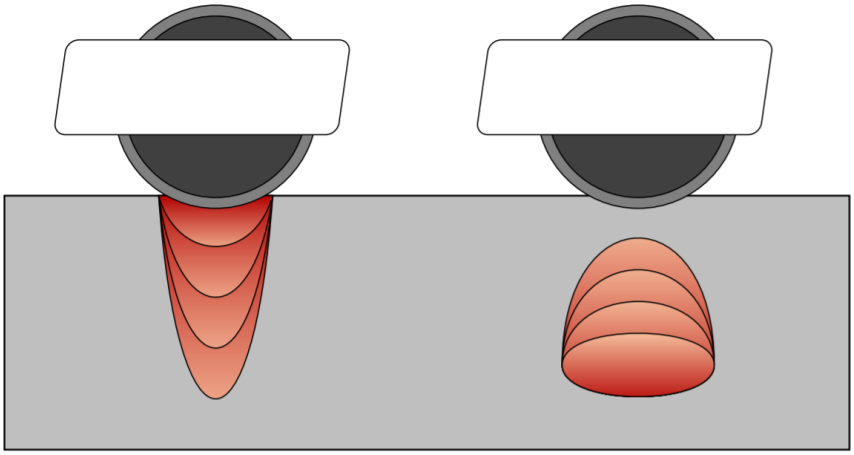

Figure 2.1: *The compacted zone grows either "from top to bottom" (left) or "from bottom to top" (right). Inside stiff beds, when the contact pressure exceeds the material strength, a compacted core zone is formed that grows upwards with every impact. This generally coincides with drum lift-off [15].*

2 Roller Compaction

The main goal of compaction theory is the understanding of how machine and material parameters affect the compaction quality. Such an understanding allows for optimisation of operational parameters based on the bed properties. This optimisation can be performed by continuous adjustment of machine parameters based on simultaneous measurement of the ground stiffness by the roller. Such Intelligent compaction systems have been developed by all leading vibratory roller manufacturers. In general, the system applies high vibration amplitude and low frequency on stiff and shallow ground, whereas low amplitude and high frequency is used on soft and deep ground. The ground stiffness affects the non-linearity of the drum-ground dynamical system, and this non-linearity can be assessed by Fourier analysis of the drum acceleration amplitudes and used as a feedback to the system [6].

2.1 Drum-ground interaction

The work of a vibratory roller is associated with the repeated cyclic application of a load on the compacted material, with the goal of achieving stiffening and permanent deformation of the particle bed. This deformation is dependent on the contact pressure and the rate of change and duration of the load [15]. Compaction quality is also highly affected by material characteristics, which in practice are often unevenly distributed within the bed [1]. Finally, the underlying layer stiffness and the water content in the bed also contribute to quality disparities [6].

The roller movement and nature of the impact determines the compaction depth, and how the compacted zone grows within the particle bed. The bed can be compacted "from top to bottom", or "from bottom to top" [15]. Figure 2.1 shows schematically how the compacted zone grows in both cases. Regarding the drum motion, one can identify a spectrum of compaction modes: continuous contact, partial uplift, double jump, rocking motion, and chaotic motion [1, 16]. Figure 2.2 shows typical contact force behaviour during continuous contact, partial uplift, and double jumps.

Continuous contact, where the roller moves vertically in a sinusoidal fashion and remains in contact with the ground, is an example of "top to bottom" compaction. The surface material is compacted first, and subsequent passes compact materials at deeper layers. The contact pressure should not exceed the strength of the material, lest particles will be squeezed out from below the roller. Still, the optimal contact pressure is close to the material strength. Since the strength increases as the material is compacted, vibratory settings must be adjusted over different passages [15].

On the other hand, the case of partial uplift is an example of discontinuous contact, which gives rise to

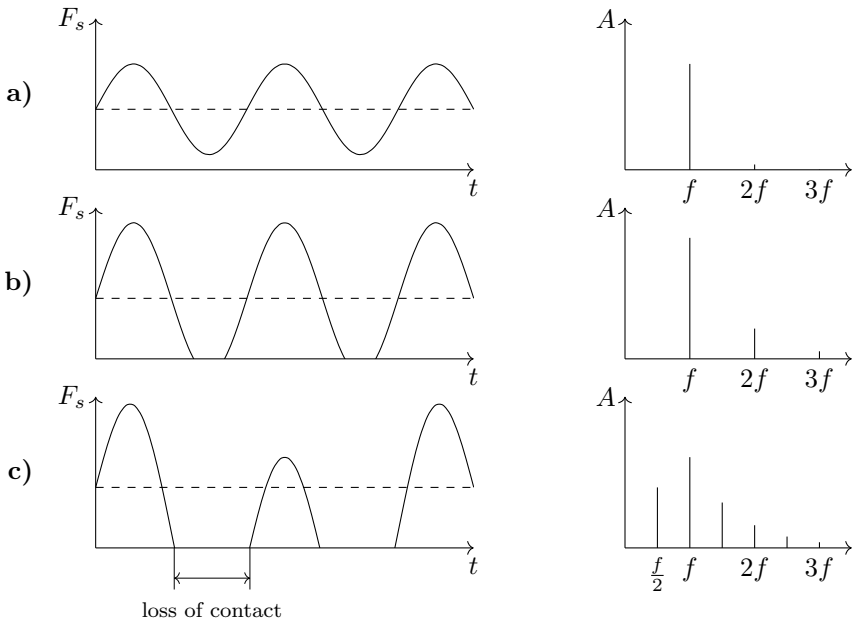

Figure 2.2: *Typical behaviour of the drum-ground contact force F_s. For low bed stiffnesses and low eccentricity of the rotating shaft (a), the contact is continuous. On stiffer beds (b), there is a periodic loss of contact as the drum makes small jumps. On even more compacted ground (c), the drum may start to bounce, rock, or perform double jumps. The behaviour can be characterised by the spectrum of acceleration frequencies (right) [16]. On stiffer beds, the vertical drum acceleration will have subharmonic components. These subharmonic frequencies are therefore used to quantify the bed stiffness in Intelligent compaction.*

"bottom to top" compaction, where the surface layer is not compacted but a core in the body of a dispersed material is packed. In that scenario, the roller lifts off the ground slightly and compacts the material upon impact, but the roller movement is still sinusoidal. In this case, a contact pressure larger than the material strength is desired [15, 1]. As an example of contact pressure influence, Kim and Chun [17] tested several non-cylindrical compactor shapes, and found that the contact area had a large influence on the compaction depth.

With larger contact pressure, the roller makes double jumps, a subharmonic vibration. The amplitudes of adjacent vibrations vary, which reduces control and compaction efficiency. Double jump is therefore an unwanted operational mode, but it can still be worth modelling. Rocking motion describes rotational vibrations of the roller around all axes, leading to an uncontrolled and finally chaotic motion [1, 16].

According to Tarasov et al. [18], the theory on vibratory drum interaction with the material still lags behind the technical roller development, and the physical processes cannot be explained with any analytical method. Simulation methods offer a possible solution. In particular, a full co-simulation of the ground and the vibratory roller could give new insights into the processes of the drum-ground interaction.

2.2 Ground stiffness estimation

In order to implement Intelligent compaction, the bed stiffness must be measured continuously so that the operational parameters can be properly adjusted. Thus, the question remains how to measure bed stiffness with the roller. One out of several proposed analysis method is to use the practical experience of drum response at varying beds to estimate the ground stiffness. Given that drum oscillations are more harmonic when compacting soft beds, the concept is based on measurement of the drum motion and analysis of the nature of its vibrations. This is realised by fitting an accelerometer to the drum. The vertical component of the drum acceleration is then fed to a software that performs a frequency analysis on the data. Based on the amplitudes of the acceleration at various frequencies, an estimation of the bed stiffness can then be derived [1, 6].

Typical acceleration spectra for different bed stiffnesses are shown to the right in Figure 2.2. On a soft

particle bed during continuous contact (a), the contact force and drum vibrations will be sinusoidal. A frequency analysis of the movement shows that the vibration displacement has only one frequency, namely the excitation frequency f. On a slightly stiffer material (b), overtones in the vibration occur at integer multiples of f, yielding a non-linear vibratory behaviour. On an even stiffer bed (c), spikes in the frequency spectrum may also occur at subharmonic values such as $f/2$, $3f/2$, $5f/2$ etc. [16]. In other words, the stiffer the bed, the larger the vibrations at overtone and subharmonic frequencies are in relation to the amplitude at the excitation frequency. This phenomenon can be used to estimate of the bed stiffness.

Several stiffness estimates based on frequency analysis have been proposed. The compaction meter value (CMV) is perhaps the most common, originally introduced by Thurner and Sandström [19] as

$$CMV = C\frac{A_{2f}}{A_f}, \tag{2.1}$$

where C is a calibration rate usually set to 300, A_f is the vibration amplitude of a subharmonic of the vertical acceleration spectrum at the nominal frequency f, and A_{2f} is the amplitude at $2f$, as obtained from a fast Fourier transform. Thus, for a fully harmonic oscillation, the CMV will be zero, but on stiff grounds, the non-linearity of the contact force will be reflected in the CMV value. This method requires careful calibration, however, as the value is also influenced by roller size, forward velocity, soil type and other factors [1, 2, 6].

In 2004, Japanese construction equipment manufacturer Sakai proposed a compaction control value (CCV) as

$$CCV = \frac{A_{0.5f} + A_{1.5f} + A_{2f} + A_{2.5f} + A_{3f}}{A_{0.5f} + A_f}, \tag{2.2}$$

where A_{kf} is the amplitude of a subharmonic of the acceleration spectrum of the drum at the frequency kf. Thus, CCV accounts for a number of additional subharmonic frequencies, compared to the CMV. These frequencies occur only under very stiff conditions [6, 20].

Alternatively, the bed stiffness can be determined by integrating the roller motion. This is known as the roller-integrated stiffness. A spring-dashpot model is applied and solved for the ground. The elastic stiffness can then be related to the unloading curve of the static force versus the vertical displacement. When the drum velocity is zero, the bed spring stiffness is given by

$$k_s = 4\pi^2 f^2 \left(M + \frac{mr_o \cos(\phi)}{z} \right), \tag{2.3}$$

where M is the drum mass, mr_o describes the eccentricity, ϕ is the phase angle, and z is the vertical drum displacement [6].

Since k_s is dependent on the area over which the load is applied, the independent modulus E_{vib} must be derived from the estimated stiffness, based on contact theory of a cylinder in contact with a half-plane [6].

Alternative analysis methods are also in use. Examples include measuring the machine drive power and calculating ground stiffness based on a drum-ground interaction model [1, 6]. These methods are not further explored here.

In this work, CMV and CCV are measured in the compaction simulations. This serves the purpose of qualitative validation of the roller model, as well as investigation of the relation between CMV, CCV, and bed material properties. If the roller model is sufficiently accurate, and the interaction with the ground is simulated correctly, subharmonic and overtone vibration frequencies should also occur in our roller model.

2.3 Prevalent simulation methods

Simulation of compaction requires a model that accounts for the bulk effects of grains of varying sizes and irregular shapes. The literature on compaction simulation can roughly be divided into three groups based on the ground model used: spring-damper models, finite element models and discrete element models. The models attempt to capture the non-linear deformation behaviour of compacted ground on different levels on complexity. In addition, some of the wealth of literature on MBS-DEM co-simulation is covered here. This literature review shows that the experience from MBS-DEM coupling could be applied to improve present compaction simulation methods.

2.3.1 Spring-damper ground models

In spring-damper models, the ground is generally regarded as a dynamical one- or two-dimensional system of springs, dashpots and masses. Such an approach is generally sufficient when the focus of the work lies on the roller movement rather than the quality of compaction. This includes studies on double-jump and rocking, as well as machine vibrations.

Pietzsch and Poppy [21] used a spring-damper system to model the ground, and applied a model of a vibratory roller to assess compaction and lift-off. A distinction between bounce and contact operation was made in the model. Lateral movement of the roller was not modelled. Still, the model was found suitable for assessment of the roller vibrations and ground compaction.

Kordestani [22] modelled the ground as a spring-damper system and the roller as a 2D multibody system, and simulated vibrations in the roller and their effects on driver comfort and compaction performance. Field measurements were also conducted to capture the vibration environment during different operational modes. Parametric analyses were performed to improve the vibration environment and compaction quality.

Imran et al. [23] modelled asphalt as a spring-damper system and simulated compaction of a moving vibratory roller. Comparison with case studies showed good agreement of results, at least for low vibration frequencies. A larger discrepancy was found for higher frequencies. The model was limited to studying vibration dynamics in the vertical direction.

2.3.2 FEM ground models

Literature on finite element compaction simulation comprises models where the granular material is approximated as a continuum divided into elements. The dynamical equations are solved under the assumption that the grain interactions can be emulated by some material model. Generally, an elastic-plastic material model is used, possibly with additional cohesive or viscous properties. Uses include modelling of compaction depth.

Pan and Selby [24] used finite element dynamics analysis to model the impact of a hammer on a particle bed. The ground was modelled as an elastic-plastic cohesive material, with axisymmetric elements about the point of impact. The pressure wave propagation in the material was then studied, and the acceleration field of elements was assessed to give a measure of the depth of compaction. Compaction depth was found to increase with the hammer weight and speed. Increased particle stiffness also led to deeper reach of the acceleration field, but decreased mass penetration. Next, multiple drops were tested, which led to increasing depths of compaction.

Kim and Chun [17] modelled the ground with a finite element mesh and used it to simulate impact roller compaction for different roller types. The shape and orientation of the impact roller affected its depth of influence. The material was represented by solid elements of elastic-plastic material. Non-cylindrical rollers had a deeper zone of influence, but the top layer remained looser.

Kenneally et al. [25] used plane strain finite element analysis for structural dynamics to explore how subgrade and base moduli affect the stiffness measured by the roller. The particulate matter was modelled as a continuous linear-elastic material because the ground was considered as fully compacted. The measurement depth of the roller was found to be about 1 m, that is, when the top layer is deeper than that, the total ground stiffness is independent of the subgrade modulus.

2.3.3 DEM ground models

Discrete element models have the advantage of avoiding the assumption of continuity by modelling every particle as a rigid body, and applying some contact model that captures the bulk behaviour of the material. DEM methods can be very computationally demanding, depending on the number of particles and the approximation of particle geometries. Particle geometry ranges from spheres, to clumps of spheres, and polyhedrons.

Zhao [11] used a 2D DEM model to simulate asphalt pavement compaction and adjust compaction parameters. Roller weight and speed were varied, and the void of coarse aggregates was measured as an index of compaction effect. It was found that a roller speed of 4 m/s was optimal with regard to the required number of passes. Optimal roller weight was found around 10 tonnes. The obtained parameters were in accordance with construction experience.

Pei and Yang [12] combined a granular 2D DEM base course with a deformable subgrade to model compaction of a bed on a geogrid, a type of reinforcing structural element in unbound road layers. The geogrid was implemented as evenly spread-out particles with long-distance interaction models, specifying the distance range. The subgrade was modelled by particles with similar long-range interaction models to the bottom level, essentially a linear elastic foundation layer but with a contact behaviour similar to that of the particles.

Particles were triangular, made up of three bonded balls, to better catch interlocking behaviour than spherical particles. The roller was modelled as a rotating solid cylinder. The long-range interaction was an efficient way of simulating the subgrade. Several passes of the roller increased the effect of the geogrid.

Zhao et al. [13] used 3D DEM to simulate soil compaction by a soil preparation machine roller on a bed of multisphere particles. Unlike in road construction, compaction of soil has generally been regarded as undesired, but experiments have shown that compaction can have a positive effect on soil water flow. Soil compaction dependence on compaction force was investigated. The compaction depth was adjusted based on the compaction force using a fuzzy controller method. The stability of compaction was improved compared to using a constant compaction depth.

2.3.4 DEM-MBS coupling

Coupling of DEM to a multibody solver is prevalent in the literature. The examples presented here cover work that has some similarity to compaction, such as bulldozing and wheel interaction with soil. This literature has served as inspiration not only on the implementation of coupling, but also on calibration methods, regulators for the motors, and the multibody modelling.

Ghorbani [26] used a DEM-multibody dynamics coupling for prediction of forces on tilling tools in soil. After calibration, simulations were run in 2D with circular particles, and a rigid pendulum whose movement was calculated in a multibody solver based on the forces obtained from contact with the particles. The resulting force and movement were compared to experiments. Although DEM greatly overestimated the impact force compared to experiments, the agreement of results was improved when using the multibody coupling.

Ghoohaki [27] coupled DEM to a multibody solver and applied it to a backhoe sand digging operation. The particles were modelled as cube-shaped clumps, comprising eight subspheres. A discharge test through an orifice and an angle of repose test were used to validate the particle model, showing good agreement with experiments. The multibody solver was based on a penalty method, with an explicit predictor-corrector time integration scheme. A high-fidelity rigid body model of the backhoe was used, including models of the track and manipulator connected with joints, and actuators following given paths using PD regulators. The multibody model was then coupled to the DEM solver as the backhoe operated on 27 000 particles of side length 0.1 m. During operation, the actuator forces were calculated.

Sane [28] developed a coupling between cohesive DEM and a multibody solver and applied it to simulate bulldozer earth levelling operations on mud. The particle model is the same as in Ghoohaki [27], but also includes cohesive effects by adding a limited contractive force when particles overlap. The excavation performance and mobility of the bulldozer was predicted.

Roy [29] validated a coupled DEM-MBD code using experiments on non-cohesive soft soil, with the same DEM and multibody framework as Ghoohaki [27] and Sane [28]. The sand-type material was again modelled with cubical particles. Material properties were calibrated with three tests: a shear cell, penetroplate pressure-sinkage, and wheel drawbar pull-torque-slip test. These tests were used to calibrate shearing, friction and shear strength, and slip, respectively. The slip test has some similarity to compaction simulations, although with focus on the wheel behaviour rather than ground compaction. The calibrated model was then applied to model a Humvee-type vehicle driving on soft soil.

Barrios and Tavares [30] coupled DEM and MBD to model high pressure roll grinding. The material is led between two rotating rolls, one with fixed translations and one with free lateral movement. A rigid body dynamics model was applied to the floating roll, which was pushed by a hydraulic system towards the fixed roll. Spherical breakable particles were used.

2.4 Coupling methods for compaction simulation

Although DEM has been successfully applied to a large range of other problems, the literature on DEM roller compaction is limited. The machine models used in the DEM compaction literature are usually restricted to a rolling cylinder with a superimposed vertical oscillating motion or force. In addition, most simulations are performed in 2D, or, if three dimensions are simulated, spherical particles are used. In reality, irregularly shaped particles lead to interlocking behaviours that cannot be captured under a spherical assumption. Good attempts have been made at relating 2D results to 3D, for instance in terms of the porosity [9], but the generalisation to 3D requires many assumptions, the validity of which is not self-evident. Further, the complexity of the internal roller geometry can affect vibration modes, and limiting the roller movement to a vertical oscillation ignores e.g. the kneading and rubbing effects of horizontal vibrations.

A wealth of literature on co-simulation of multibody dynamics and DEM is available, and impressive results have been achieved. Several phenomena with some similarity to roller compaction have been studied in detail, such as wheel-soil interaction and roll grinding. However, little attention has been paid to application of multibody dynamics to a vibratory roller in a DEM framework. As a result, existing simulation methods can not fully capture the complex interplay between roller dynamics and the non-linear response of the particulate material in the bed. Hence, augmented models are required to broaden the range of compaction behaviour that can be successfully captured in simulations.

The purpose of this thesis is to develop a new simulation method, that applies the promising and well-documented MBS-DEM coupling approach to roller compaction. To this end, a multisphere DEM model is used to model the UGMs, in combination with a multibody machine model. All steps necessary to enable such a coupled simulation are covered in detail in this thesis. The resulting co-simulation represents a higher level of detail than has previously been achieved within the field of DEM roller compaction.

Figure 3.1: *Dynapac CA3500D single drum vibratory roller, the machine used in the experiments and modelled in the multibody solver. Reproduced with permission from Dynapac.*

3 Multibody Roller Modelling

This chapter covers the theory and implementation of a solver for constrained systems of rigid bodies, and the steps in creating a multibody model of the roller. The solver automatically formulates and solves an equation system based on user input of an arbitrary number of bodies, constraints, and loads. The module also supports positioning according to constraints as well as simple visualisation.

Based on drawings and CAD files of the vibratory roller, a representative multibody system is derived. An analysis of the mechanical system indicates that the machine parts can be grouped into in a set of five rigid bodies. The masses and inertia tensors of these bodies are extracted from the CAD model by combining the properties of all the components included in each body. This system of bodies, constraints, and loads is then implemented in the multibody solver.

The machine used in the experiments is Dynapac's CA3500D model, shown in Figure 3.1.

3.1 Constrained rigid body dynamics

The motion of the dynamical system is obtained by solution of the Newton-Euler equations with a Lagrange formulation of constraints. Body orientations are formulated as quaternions. Three translational degrees of freedom can be locked with a spherical joint, and three rotational degrees of freedom can be locked with what is here referred to as a slider joint. Any joint type, such as a pin joint or fixed constraint, can then be created by appropriate combination of these six constraint equations. The method for the multibody formulation is a synthesis based on various literature and new work. The general formulation of the constrained equations of motion is taken from Shabana [31]. The explicit formulation of the spherical joints and coordinate systems is from Stoneking [32]. Further, the method of state vector transformation is inspired by Chappuis [33]. In the present work, the expressions for the single- and multiaxial springs and dampers are derived, and a solution algorithm is set up. For the rotational degrees of freedom, a purely analytical but versatile slider constraint is introduced, rather than defining a wider range of various mechanical joints and deriving the equations for each constraint type.

3.1.1 Newton-Euler equations

The multibody solver models n_b bodies with a total of n degrees of freedom, and solves the equations of motion:

$$\boldsymbol{M}\ddot{\boldsymbol{q}} = \boldsymbol{Q}, \tag{3.1}$$

where $\boldsymbol{M}$ is a mass matrix $(n \times n)$, $\boldsymbol{q} = \begin{bmatrix} \boldsymbol{r}_1^\top & \boldsymbol{\theta}_1^\top & \dots & \boldsymbol{r}_m^\top & \boldsymbol{\theta}_m^\top \end{bmatrix}^\top$ are the generalised coordinates $(n \times 1)$ describing translation $\boldsymbol{r}$ and rotation $\boldsymbol{\theta}$ of each body, and $\boldsymbol{Q}$ is a vector $(n \times 1)$ of generalised loads. The dot denotes differentiation with respect to time. In the Newton-Euler version of the equations of motion, the system is formulated for each body i as

$$\begin{bmatrix} m_i \mathbf{1} & \mathbf{0} \\ \mathbf{0} & \boldsymbol{I}_i \end{bmatrix} \begin{bmatrix} \dot{\boldsymbol{v}}_i \\ \dot{\boldsymbol{\omega}}_i \end{bmatrix} = \begin{bmatrix} \boldsymbol{Q}_i^r \\ \boldsymbol{Q}_i^\theta - \boldsymbol{\omega}_i \times (\boldsymbol{I}_i \boldsymbol{\omega}_i) \end{bmatrix}. \tag{3.2}$$

Here, the velocity $\boldsymbol{v}_i = \dot{\boldsymbol{r}}_i$, and the angular velocity $\boldsymbol{\omega}_i = \dot{\boldsymbol{\theta}}_i$. m_i is the mass, $\mathbf{1}$ denotes the 3×3 identity matrix, and $\boldsymbol{I}_i$ is the inertia tensor. The mass matrices and generalised loads of each body are then assembled into $\boldsymbol{M}$ and $\boldsymbol{Q}$.

Since each body has six degrees of freedom, its state in space can be fully described by six coordinates: three translations and three rotations. If three Euler angles (consecutive rotations about three axes) are used to describe the rotation, there is a risk that the system rotates to a state where two of the rotation axes become parallel, known as gimbal lock. In order to avoid gimbal lock, a fourth rotational parameter is introduced via quaternions.

3.1.2 Quaternions

The quaternion formulation is based on Graf [34]. An arbitrary rotation in space can be described by four parameters p_0, p_1, p_2, p_3, under the constraint

$$\sum_{i=0}^{3} p_i^2 = 1. \tag{3.3}$$

Given an angular velocity $\boldsymbol{\omega}$ in global coordinates, i.e., in a fixed reference frame, the relationship between $\boldsymbol{\omega}$ and the rate of change of the vector $\boldsymbol{p} = \begin{bmatrix} p_0 & p_1 & p_2 & p_3 \end{bmatrix}^\top$ can be obtained as

$$\dot{\boldsymbol{p}} = \frac{1}{2} \boldsymbol{E}^\top \boldsymbol{\omega}, \quad \boldsymbol{\omega} = 2 \boldsymbol{E} \dot{\boldsymbol{p}}. \tag{3.4}$$

Similarly, given a rotation $\bar{\boldsymbol{\omega}}$ in *local* coordinates pertaining to a moving body, the corresponding relationship is

$$\dot{\boldsymbol{p}} = \frac{1}{2} \boldsymbol{G}^\top \bar{\boldsymbol{\omega}}, \quad \bar{\boldsymbol{\omega}} = 2 \boldsymbol{G} \dot{\boldsymbol{p}}. \tag{3.5}$$

The matrices $\boldsymbol{E}(\boldsymbol{p})$ and $\boldsymbol{G}(\boldsymbol{p})$ are given by

$$\boldsymbol{E} = \begin{bmatrix} -p_1 & p_0 & -p_3 & p_2 \\ -p_2 & p_3 & p_0 & -p_1 \\ -p_3 & -p_2 & p_1 & p_0 \end{bmatrix}, \quad \boldsymbol{G} = \begin{bmatrix} -p_1 & p_0 & p_3 & -p_2 \\ -p_2 & -p_3 & p_0 & p_1 \\ -p_3 & p_2 & -p_1 & p_0 \end{bmatrix}, \tag{3.6}$$

where it can be noted that $\boldsymbol{E}\boldsymbol{E}^\top = \boldsymbol{G}\boldsymbol{G}^\top = \mathbf{1}$.

A position $\bar{\boldsymbol{x}}$ in the local coordinate system is transformed to the global inertial system as

$$\boldsymbol{x} = \boldsymbol{R} \bar{\boldsymbol{x}}, \quad \bar{\boldsymbol{x}} = \boldsymbol{R}^\top \boldsymbol{x}, \tag{3.7}$$

and for quaternions the rotation matrix $\boldsymbol{R}$ is obtained as

$$\boldsymbol{R} = \boldsymbol{E}\boldsymbol{G}^\top. \tag{3.8}$$

The quaternion defining a rotation ϕ around a normal vector $\boldsymbol{n}$ is obtained as

$$p_0 = \cos \frac{\phi}{2}, \quad p_i = n_i \sin \frac{\phi}{2} \, (i = 1, 2, 3). \tag{3.9}$$

The use of quaternions introduces an additional degree of freedom for each body, which means that the total number n of coordinates increases from $6m$ to $7m$. The constraint in Equation 3.3 ensures that the number of free degrees of freedom remains limited to $6m$. For a more in-depth review of quaternions, see Graf [34].

3.1.3 Equation system with constraints

The bodies are generally connected by constraints, such as joints or prescribed motion. These constraints are described by constraint equations,

$$\boldsymbol{C}(\boldsymbol{q}, \dot{\boldsymbol{q}}, t) = \boldsymbol{0}. \tag{3.10}$$

The constraint equations guarantee that certain degrees of freedom of pairs of bodies are related. Each constraint equation reduces the number of free degrees of freedom of the multibody system by one. Constraints can be set on the generalised coordinates $\boldsymbol{q}$ (geometric constraints) or on their time derivative $\dot{\boldsymbol{q}}$ (kinematic constraints).

In order to solve the Newton-Euler equations subject to n_c constraints, we must either reduce the number of equations of motion by n_c, or expand the system in Equation 3.1 with a differentiated form of the constraint equations and solve for the resulting constraint forces. The first approach is fast, but it has the disadvantage that one must determine which coordinates are independent and dependent in a systematic way. In this implementation, generality is prioritised over speed, and so the second approach is implemented with a Lagrange multiplier scheme.

In other terms, we have the second order ordinary differential Newton-Euler equations, in combination with the constraint equations, which are algebraic equations if the constraints are geometric. The combination therefore constitutes a semi-explicit differential-algebraic equation (DAE). Here, this system of equations is solved with index reduction, where the constraint equations are differentiated and added to the Newton-Euler system. The risk with index reduction is that over time, constraints may no longer be fulfilled, since the constraint equation is formulated for the acceleration of bodies rather than their position. In addition, all bodies must initially be placed so that they fulfil all constraints with regard both to position and velocity. The problems can be alleviated by application of a different numerical technique for the solution of DAEs. An implicit integration scheme can be used in conjunction with stabilisation methods (e.g. [35]). Indeed, Chappuis [33] used a bias velocity vector, that allows for the constraint forces to perform some work to counter position drift. This is also known as Baumgarte stabilisation, but the method has not been implemented in this work.

Next, the geometric constraint equations $\boldsymbol{C}(\boldsymbol{q}(t), t)$ must be formulated in the velocities $\ddot{\boldsymbol{q}}$, so that the constraints can be added to the Newton-Euler system. To this end, $\boldsymbol{C}$ is differentiated twice with regard to time:

$$\frac{\mathrm{d}}{\mathrm{d}t}\boldsymbol{C} = \frac{\partial}{\partial t}\boldsymbol{C} + \frac{\partial \boldsymbol{C}}{\partial \boldsymbol{q}}\dot{\boldsymbol{q}} = \boldsymbol{0}. \tag{3.11}$$

$$\frac{\mathrm{d}^2}{\mathrm{d}t^2}\boldsymbol{C} = \frac{\partial^2}{\partial t^2}\boldsymbol{C} + 2\frac{\partial^2 \boldsymbol{C}}{\partial \boldsymbol{q}\partial t}\dot{\boldsymbol{q}} + \frac{\partial \boldsymbol{C}}{\partial \boldsymbol{q}}\ddot{\boldsymbol{q}} + \frac{\partial}{\partial \boldsymbol{q}}\left(\frac{\partial \boldsymbol{C}}{\partial \boldsymbol{q}}\dot{\boldsymbol{q}}\right)\dot{\boldsymbol{q}} = \boldsymbol{0}. \tag{3.12}$$

Here, $\frac{\partial \boldsymbol{C}}{\partial \boldsymbol{q}} = \boldsymbol{J}$ is the Jacobian matrix $(n_c \times n)$ of the vector of constraint equations with regard to the generalised coordinates. Defining $\boldsymbol{Q}^c = -\frac{\partial^2}{\partial t^2}\boldsymbol{C} - 2\frac{\partial^2 \boldsymbol{C}}{\partial \boldsymbol{q}\partial t}\dot{\boldsymbol{q}} - \frac{\partial}{\partial \boldsymbol{q}}\left(\frac{\partial \boldsymbol{C}}{\partial \boldsymbol{q}}\dot{\boldsymbol{q}}\right)\dot{\boldsymbol{q}}$ as the vector $(n_c \times 1)$ of force terms that arise from the differentiation of $\boldsymbol{C}$, the system of equations can be expanded as

$$\begin{bmatrix} \boldsymbol{M} & \boldsymbol{J}^\top \\ \boldsymbol{J} & \boldsymbol{0} \end{bmatrix} \begin{bmatrix} \ddot{\boldsymbol{q}} \\ \boldsymbol{\lambda} \end{bmatrix} = \begin{bmatrix} \boldsymbol{Q} \\ \boldsymbol{Q}^c \end{bmatrix}. \tag{3.13}$$

$\boldsymbol{\lambda}$ is a vector $(n_c \times 1)$ of Lagrange multipliers, which correspond to the generalised constraint forces. In this implementation, our constraints will not explicitly depend on time, so only the last term in $\boldsymbol{Q}^c$ remains. Before solution, the matrix $\boldsymbol{J}$ and vector $\boldsymbol{Q}^c$ must be assembled from the equations pertaining to each constraint. The expressions must be derived for each type of constraint and formulated in appropriate coordinate systems. Note that since the right-hand side of Equation 3.13 depends on both $\boldsymbol{q}$ and $\dot{\boldsymbol{q}}$, an explicit form of the equations cannot be obtained.

Coordinate systems

In the Newton-Euler equations, it is natural to describe the translational velocities in the inertial frame of reference, and the rotational velocities in the local coordinate systems. This simplifies the formulation of the inertia tensor, which is fixed only in the local system. The constraint equations must be formulated in an appropriate system as well, with the generalised coordinates properly transformed. The appropriate choice of the constraint coordinate system depends on the nature of the constraint. In the simplest case, the constraint

equations are all formulated in the global system. For each body i, the constrained system of equations is then

$$\begin{bmatrix} m_i\mathbf{1} & \mathbf{0} & (\boldsymbol{J}_i^r)^\top \\ \mathbf{0} & \bar{\boldsymbol{I}}_i & (\boldsymbol{R}_i\boldsymbol{J}_i^\theta)^\top \\ \boldsymbol{J}_i^r & \boldsymbol{R}_i\boldsymbol{J}_i^\theta & \mathbf{0} \end{bmatrix} \begin{bmatrix} \dot{\boldsymbol{v}}_i \\ \dot{\bar{\boldsymbol{\omega}}}_i \\ \boldsymbol{\lambda} \end{bmatrix} = \begin{bmatrix} \boldsymbol{Q}_i^r \\ \boldsymbol{Q}_i^\theta - \bar{\boldsymbol{\omega}}_i \times (\bar{\boldsymbol{I}}_i\bar{\boldsymbol{\omega}}_i) \\ \boldsymbol{R}_i\bar{\boldsymbol{Q}}_i^c \end{bmatrix}, \tag{3.14}$$

where quantities in the local coordinate system are written with a bar above, and the derivatives of the constraint equations with regard to the rotational degrees of freedom have been transformed to the global system. Such a system is typical of spherical constraints, as is the formulation of $\boldsymbol{Q}^c$ in the local system. The matrix $\boldsymbol{J}_i$ here refers to the columns in $\boldsymbol{J}$ that correspond to the degrees of freedom of body i. On the other hand, each row of $\boldsymbol{J}$ reduces the total number of degrees of freedom by one. At this point, all that remains is to derive $\boldsymbol{J}^{(j)}$ and $\boldsymbol{Q}^{c,(j)}$ for different constraint types j.

Spherical joint

A spherical joint prescribes coincidence of two points, and allows for free rotations. It therefore constrains three degrees of freedom and can be described by a system $\boldsymbol{C} = \mathbf{0}$ of three constraint equations. Describing the joint coordinates in the global system, we have

$$-\boldsymbol{r}_1 - \boldsymbol{u}_1 + \boldsymbol{r}_2 + \boldsymbol{u}_2 = \mathbf{0}, \tag{3.15}$$

where $\boldsymbol{u}_i$ is the position of the joint with regard to the position of body i, defined in the inertial frame. Time-differentiating twice yields

$$-\dot{\boldsymbol{r}}_1 - \boldsymbol{\omega}_1 \times \boldsymbol{u}_1 + \dot{\boldsymbol{r}}_2 + \boldsymbol{\omega}_2 \times \boldsymbol{u}_2 = \mathbf{0}, \tag{3.16}$$

$$-\ddot{\boldsymbol{r}}_1 - \dot{\boldsymbol{\omega}}_1 \times \boldsymbol{u}_1 - \boldsymbol{\omega}_1 \times \boldsymbol{\omega}_1 \times \boldsymbol{u}_1 + \ddot{\boldsymbol{r}}_2 + \dot{\boldsymbol{\omega}}_2 \times \boldsymbol{u}_2 + \boldsymbol{\omega}_2 \times \boldsymbol{\omega}_2 \times \boldsymbol{u}_2 = \mathbf{0}. \tag{3.17}$$

Since these equations are basis-free, let us now formulate relevant quantities in Equation 3.17 in their appropriate bases, and transform all terms to the inertial system:

$$-\ddot{\boldsymbol{r}}_1 - \boldsymbol{R}_1(\dot{\bar{\boldsymbol{\omega}}}_1 \times \bar{\boldsymbol{u}}_1) - \boldsymbol{R}_1(\bar{\boldsymbol{\omega}}_1 \times \bar{\boldsymbol{\omega}}_1 \times \bar{\boldsymbol{u}}_1) + \ddot{\boldsymbol{r}}_2 + \boldsymbol{R}_2(\dot{\bar{\boldsymbol{\omega}}}_2 \times \bar{\boldsymbol{u}}_2) + \boldsymbol{R}_2(\bar{\boldsymbol{\omega}}_2 \times \bar{\boldsymbol{\omega}}_2 \times \bar{\boldsymbol{u}}_2) = \mathbf{0}. \tag{3.18}$$

For a matrix formulation of this equation set, it is convenient to introduce the skew-symmetric matrix equivalent of the cross product and the double cross product, as

$$[\boldsymbol{v}]_\times = \begin{bmatrix} 0 & -v_3 & v_2 \\ v_3 & 0 & -v_1 \\ -v_2 & v_1 & 0 \end{bmatrix}, \quad [\boldsymbol{v}]_{\times\times} = \begin{bmatrix} -v_2^2 - v_3^2 & v_1v_2 & v_1v_3 \\ v_2v_1 & -v_3^2 - v_1^2 & v_2v_3 \\ v_3v_1 & v_3v_2 & -v_1^2 - v_2^2 \end{bmatrix}, \tag{3.19}$$

with the properties

$$[\boldsymbol{v}]_\times \boldsymbol{w} = \boldsymbol{v} \times \boldsymbol{w}, \quad [\boldsymbol{v}]_{\times\times} \boldsymbol{w} = \boldsymbol{v} \times \boldsymbol{v} \times \boldsymbol{w}. \tag{3.20}$$

Now, we may rewrite Equation 3.18 as

$$\underbrace{\begin{bmatrix} -\mathbf{1} & -\boldsymbol{R}_1[\bar{\boldsymbol{u}}_1]_\times^\top & \mathbf{1} & \boldsymbol{R}_2[\bar{\boldsymbol{u}}_2]_\times^\top \end{bmatrix}}_{\boldsymbol{J}^{(\mathrm{sph})}} \begin{bmatrix} \dot{\boldsymbol{v}}_1 \\ \dot{\bar{\boldsymbol{\omega}}}_1 \\ \dot{\boldsymbol{v}}_2 \\ \dot{\bar{\boldsymbol{\omega}}}_2 \end{bmatrix} = \underbrace{\begin{bmatrix} \boldsymbol{R}_1[\bar{\boldsymbol{\omega}}_1]_{\times\times}\bar{\boldsymbol{u}}_1 - \boldsymbol{R}_2[\bar{\boldsymbol{\omega}}_2]_{\times\times}\bar{\boldsymbol{u}}_2 \end{bmatrix}}_{\boldsymbol{Q}^{c,(\mathrm{sph})}}, \tag{3.21}$$

and the matrices $\boldsymbol{J}^{(\mathrm{sph})}$ and $\boldsymbol{Q}^{c,(\mathrm{sph})}$ can be assembled into Equation 3.13.

Slider joint

A slider joint constrains rotation between two bodies about one or several axes. By constraining two axes and combining the slider joint with a spherical joint, a revolute joint with one rotational degree of freedom is obtained. By constraining three independent rotation axes and combining with a spherical joint, a fixed constraint is obtained with zero degrees of freedom. For the slider joint, the system of j constraint equations is defined for the angular velocities:

$$-\boldsymbol{A}^\top \boldsymbol{\omega}_1 + \boldsymbol{A}^\top \boldsymbol{\omega}_2 = \mathbf{0}, \tag{3.22}$$

where $\boldsymbol{A}$ is a matrix $(3 \times j)$ whose orthonormal columns define the constrained axes. Differentiation yields

$$-\boldsymbol{A}^\top [\boldsymbol{\omega}]_\times^\top \boldsymbol{\omega}_1 - \boldsymbol{A}^\top \dot{\boldsymbol{\omega}}_1 + \boldsymbol{A}^\top [\boldsymbol{\omega}]_\times^\top \boldsymbol{\omega}_2 + \boldsymbol{A}^\top \dot{\boldsymbol{\omega}}_2 = \boldsymbol{0}. \tag{3.23}$$

Here, $\boldsymbol{\omega}$ describes the rotational velocity of whichever system is used to define $\boldsymbol{A}$. For a revolute joint, usually the free axis of rotation must follow one of the bodies. Therefore, $\boldsymbol{A}$ is formulated in the local coordinate system of body 1, i.e. $\boldsymbol{\omega} = \bar{\boldsymbol{\omega}}_1$, and all body 2 quantities are transformed to the system of body 1 via $\boldsymbol{R}_{2\to1} = \boldsymbol{R}_1^\top \boldsymbol{R}_2$.

$$-\bar{\boldsymbol{A}}^\top \dot{\bar{\boldsymbol{\omega}}}_1 + \bar{\boldsymbol{A}}^\top [\bar{\boldsymbol{\omega}}_1]_\times^\top \boldsymbol{R}_{2\to1} \bar{\boldsymbol{\omega}}_2 + \bar{\boldsymbol{A}}^\top \boldsymbol{R}_{2\to1} \dot{\bar{\boldsymbol{\omega}}}_2 = \boldsymbol{0}, \tag{3.24}$$

where we used $[\bar{\boldsymbol{\omega}}_1]_\times^\top \bar{\boldsymbol{\omega}}_1 = \boldsymbol{0}$. In matrix form,

$$\underbrace{\begin{bmatrix} \boldsymbol{0} & -\bar{\boldsymbol{A}}^\top & \boldsymbol{0} & \bar{\boldsymbol{A}}^\top \boldsymbol{R}_1^\top \boldsymbol{R}_2 \end{bmatrix}}_{\boldsymbol{J}^{(\text{slider})}} \begin{bmatrix} \dot{\boldsymbol{v}}_1 \\ \dot{\bar{\boldsymbol{\omega}}}_1 \\ \dot{\boldsymbol{v}}_2 \\ \dot{\bar{\boldsymbol{\omega}}}_2 \end{bmatrix} = \underbrace{\begin{bmatrix} \bar{\boldsymbol{A}}^\top [\bar{\boldsymbol{\omega}}_1]_\times \boldsymbol{R}_1^\top \boldsymbol{R}_2 \bar{\boldsymbol{\omega}}_2 \end{bmatrix}}_{\boldsymbol{Q}^{c,(\text{slider})}}. \tag{3.25}$$

Spring and damper

A one-dimensional spring of stiffness k can be added between two points, that exerts a contraction force relative to the displacement of the points. The spring is strictly speaking not a constraint, since it does not reduce the number of degrees of freedom. Instead it can be implemented as a load. One then adds the force $\boldsymbol{F}_k$ to the generalised load $\boldsymbol{Q}$ as

$$\boldsymbol{F}_k = -k(\boldsymbol{r}_1 + \boldsymbol{R}_1 \bar{\boldsymbol{u}}_1 - \boldsymbol{r}_2 - \boldsymbol{R}_2 \bar{\boldsymbol{u}}_2), \tag{3.26}$$

$$\begin{bmatrix} \boldsymbol{Q}_1^r \\ \boldsymbol{Q}_1^\theta \\ \boldsymbol{Q}_2^r \\ \boldsymbol{Q}_2^\theta \end{bmatrix} = \begin{bmatrix} \boldsymbol{F}_k \\ [\bar{\boldsymbol{u}}_1]_\times \boldsymbol{R}_1^\top \boldsymbol{F}_k \\ -\boldsymbol{F}_k \\ -[\bar{\boldsymbol{u}}_2]_\times \boldsymbol{R}_2^\top \boldsymbol{F}_k \end{bmatrix}. \tag{3.27}$$

The generalised load vector for a one-dimensional damper with viscosity c is obtained similarly, with the damper force

$$\boldsymbol{F}_c = -c(\boldsymbol{v}_1 + \boldsymbol{R}_1 [\bar{\boldsymbol{\omega}}_1]_\times \bar{\boldsymbol{u}}_1 - \boldsymbol{v}_2 - \boldsymbol{R}_2 [\bar{\boldsymbol{\omega}}_2]_\times \bar{\boldsymbol{u}}_2), \tag{3.28}$$

and the assembly into $\boldsymbol{Q}$ follows Equation 3.27.

Multiaxial spring

Just like a linear spring, a multiaxial spring that has different stiffnesses in the horizontal and vertical directions can be added as a load between two points. This spring has one stiffness k_n in the normal direction, and one stiffness k_t, that is equal in all directions in the tangential plane. The normal direction $\boldsymbol{n}$ must be defined in a proper coordinate system. Here, we choose the local coordinate system of body 1 to define the normal $\bar{\boldsymbol{n}}$. The force $\boldsymbol{F}_k$ is given by

$$\boldsymbol{F}_k = -k_n \Delta \boldsymbol{r}_n - k_t \Delta \boldsymbol{r}_t \tag{3.29}$$

where the normal displacement $\Delta \boldsymbol{r}_n$ and tangential displacement $\Delta \boldsymbol{r}_t$ are given by

$$\begin{aligned} \Delta \boldsymbol{r} &= \boldsymbol{r}_1 + \boldsymbol{R}_1 \bar{\boldsymbol{u}}_1 - \boldsymbol{r}_2 - \boldsymbol{R}_2 \bar{\boldsymbol{u}}_2, \\ \Delta \boldsymbol{r}_n &= (\boldsymbol{R}_1 \bar{\boldsymbol{n}})^\top \Delta \boldsymbol{r} \boldsymbol{R}_1 \bar{\boldsymbol{n}}, \\ \Delta \boldsymbol{r}_t &= \Delta \boldsymbol{r} - \Delta \boldsymbol{r}_n. \end{aligned} \tag{3.30}$$

The force is added to the load vector as in Equation 3.27.

3.1.4 State vector transformation

In order to include the quaternion description, we solve the system in Equation 3.13 for the second derivative of the $6m \times 1$ angle-formulated generalised coordinates

$$\boldsymbol{q} = \begin{bmatrix} \boldsymbol{r}_1^\top & \boldsymbol{\theta}_1^\top & \dots & \boldsymbol{r}_m^\top & \boldsymbol{\theta}_m^\top \end{bmatrix}^\top, \tag{3.31}$$

and then transform it to the $7m \times 1$ quaternion-formulated coordinates

$$\boldsymbol{s} = \begin{bmatrix} \boldsymbol{r}_1^\top & \boldsymbol{p}_1^\top & \dots & \boldsymbol{r}_m^\top & \boldsymbol{p}_m^\top \end{bmatrix}^\top \tag{3.32}$$

The orientational state $\boldsymbol{\theta}_i$ has no practical interpretation; its definition is $\dot{\boldsymbol{\theta}}_i = \boldsymbol{\omega}_i$. Still, it is convenient to use the angle-formulated generalised coordinates since all constraints and forces are derived in terms of $\boldsymbol{\omega}$. We may formulate a 7×6 transformation matrix $\boldsymbol{S}$ between the angle and quaternion forms as

$$\underbrace{\begin{bmatrix} \dot{\boldsymbol{r}}_i \\ \dot{\boldsymbol{p}}_i \end{bmatrix}}_{\dot{\boldsymbol{s}}_i} = \underbrace{\begin{bmatrix} \boldsymbol{1} & \boldsymbol{0} \\ \boldsymbol{0} & \frac{1}{2}\boldsymbol{G}^\top(\boldsymbol{p}_i) \end{bmatrix}}_{\boldsymbol{S}_i} \underbrace{\begin{bmatrix} \boldsymbol{v}_i \\ \bar{\boldsymbol{\omega}}_i \end{bmatrix}}_{\dot{\boldsymbol{q}}_i}, \tag{3.33}$$

where it should be noted that $\boldsymbol{S}_i = \boldsymbol{S}_i(\boldsymbol{s}_i)$. After updating $\boldsymbol{s}$, one has to verify that the norm of $\boldsymbol{p}_i$ remains equal to unity, either by directly normalising it for each body or by introducing a constraint in a Lagrange multiplier fashion. Both have been tested in this implementation with no difference in results recorded. Therefore, direct normalisation is chosen for its relative simplicity.

3.2 Machine specifications

Next, a multibody model based on the elements described above is created for the machine. The CA3500D is a medium-heavy single drum vibratory roller, with an operating mass of 11.9 tonnes. It consists of a front module weighing 7.6 tonnes, and a back module of 4.5 tonnes, attached with a steering hitch. The drum is suspended in the front frame with shock absorbers. The vibration is brought about by a shaft with attached eccentric weights that rotate inside cartridges bolted to the drum [36]. An exploded view of the drum is displayed in Figure 3.2 and Figure 3.3.

The static linear load – the front module mass distributed over the drum width – is 35 kg/cm. The drum has a diameter of 1500 mm and a width of 2130 mm. During compaction, the speed is typically 1 m/s. The forward motion is driven by a turbo diesel engine connected to the back wheels, but the drum also has a motor to regulate rotation. The rotation is regulated to avoid slip between the drum and the ground. The drum has two vibratory modes of operation that result in a nominal drum oscillation amplitude of either 1.9 mm or 0.9 mm, at 30 Hz. The shaft is driven by a hydraulic motor, and the vibratory mode is changed by switching the motor's direction of rotation. The model has Intelligent compaction capabilities [38].

3.3 Modelling assumptions

By functional analysis of the front module system, ten main components are identified, connected by bearings, shock absorbers, and bolted joints. Figure 3.4 shows the schematic functional structure. The front frame is attached to the back frame via the steering hitch, and the drum motor is bolted to the front frame. The drum motor drives the driving disc (No. 9 in Figure 3.2), in which the drum (No. 1) is suspended on the left side with eight shock absorbers. The right side of the drum is attached with a bearing to a bracket (15), suspended with six shock absorbers in the front frame. The cartridges (27, 28) are bolted to the drum and the eccentric shaft (25, weights not shown) can rotate freely, with the weights rotating inside the cartridges. The vibration motor, which drives the eccentric shaft, is attached to the bracket. Thus, three main systems are rotating independently around the drum axis: (a) the front frame and bracket, (b) the drum, driving disc and cartridges, and (c) the eccentric shaft.

The rigid body model is based on the functional structure. There is no gain in modelling bolted components separately, but the spring behaviour of the shock absorbers must be captured. Therefore, the drum system is modelled with a total of 5 rigid bodies: the frame, driving disc, bracket, drum, and eccentric shaft. The mass, inertia tensors and mass centres of the bodies are derived by combining the physical properties of the

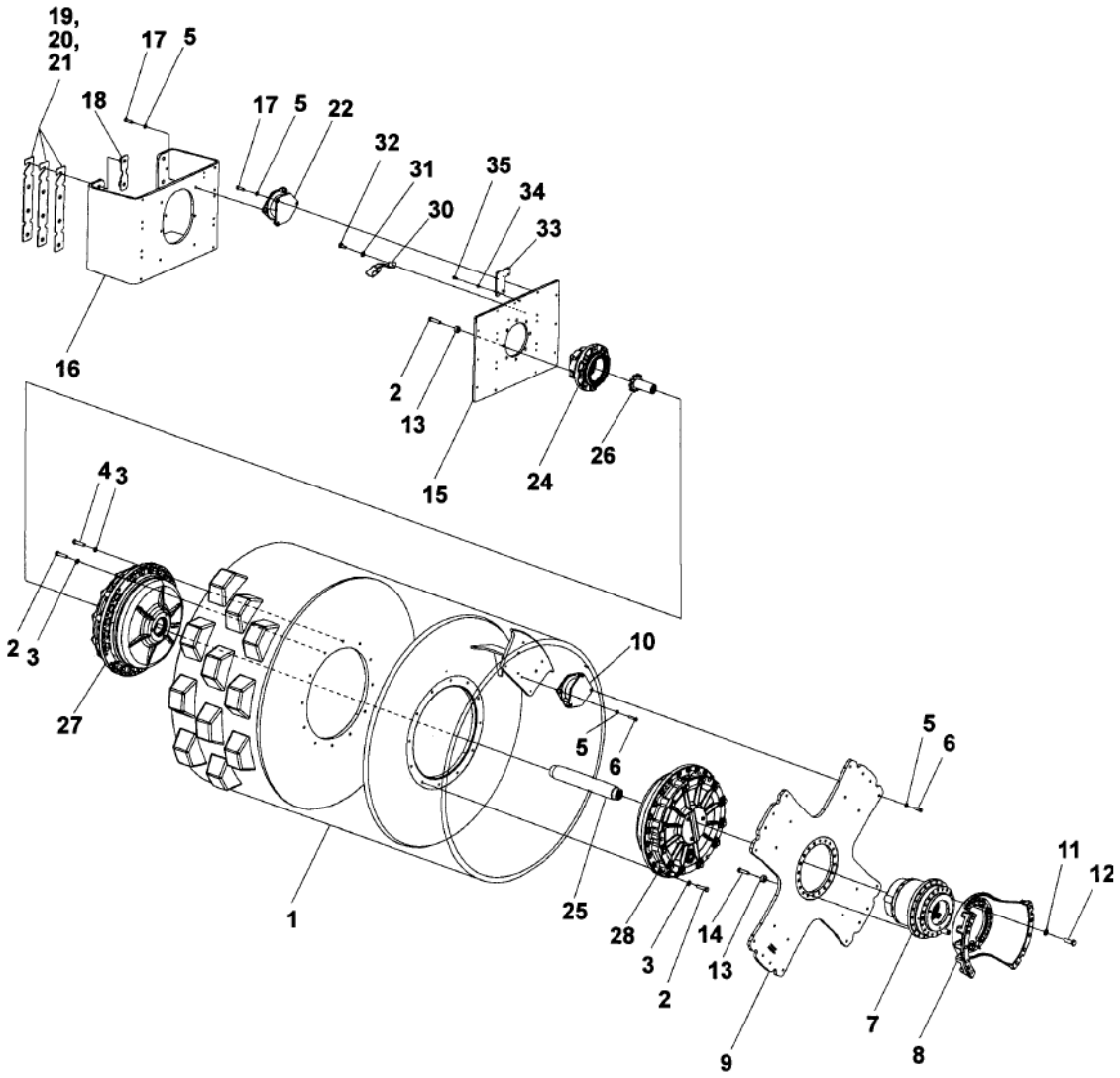

Figure 3.2: *Exploded view of the drum. The shock absorbers (10, 22) are of particular importance for a multibody model, as is the eccentric shaft (25) causing the oscillation. Figure 3.3 shows one of the cartridges (27) and the eccentric weights. Reproduced with permission from [37].*

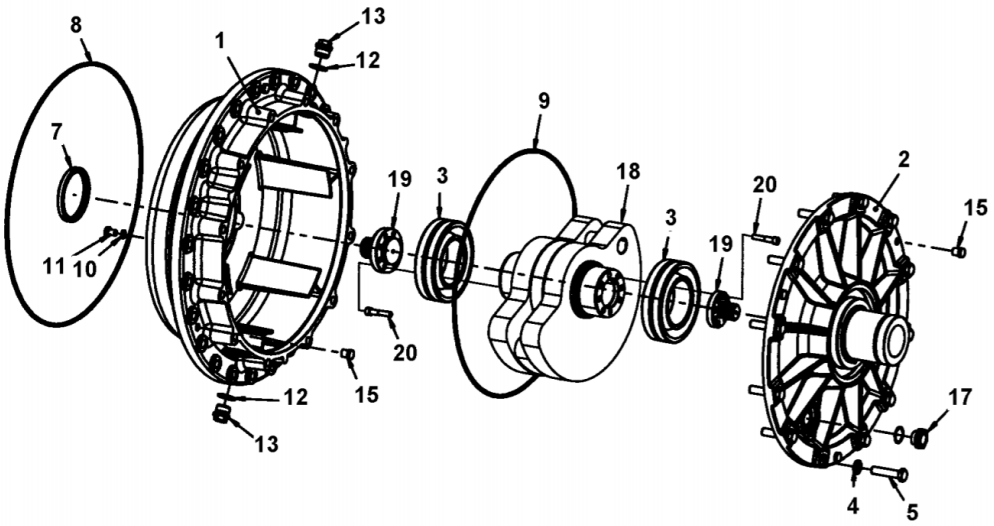

Figure 3.3: *Exploded view of the cartridge on the vibration side. The rotation of the eccentric weight (18) is what causes the drum vibrations. Reproduced with permission from [37].*

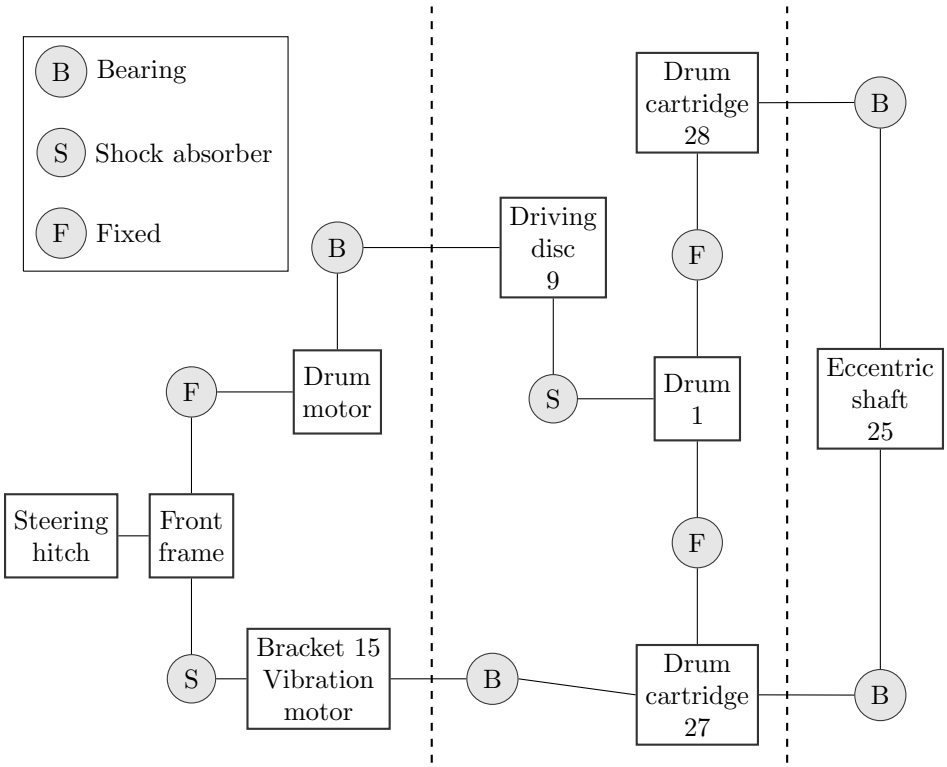

Figure 3.4: *Functional structure of the front frame and roller. Three subsystems are identified by dashed lines: the frame, the roller, and the eccentric shaft. The components correspond approximately to the numbered parts in Figure 3.2.*

Table 3.1: Dynamical properties of the five rigid bodies in the multibody model. All positions are in the global coordinate system, centred in the drum's rotational axis and the symmetric plane of the front frame. x is the direction of motion of the machine, y is parallel to the axis of rotation of the drum and z is vertical.

	Mass [kg]	Inertia tensor [kgm^2]	Mass centre [mm]
Frame	3159.0	$\begin{bmatrix} 2300 & 15 & -270 \\ 15 & 3000 & -4 \\ -270 & -4 & 5000 \end{bmatrix}$	[-69, -18, 49]
Driving disc	220.4	$\begin{bmatrix} 19 & 0 & 0 \\ 0 & 37 & 0 \\ 0 & 0 & 19 \end{bmatrix}$	[0, 782, 0]
Bracket	108.2	$\begin{bmatrix} 4 & 1 & 0 \\ 1 & 6 & 0 \\ 0 & 0 & 6 \end{bmatrix}$	[7, -649, -13]
Drum	3765.8	$\begin{bmatrix} 2100 & 0 & 0 \\ 0 & 1700 & 0 \\ 0 & 0 & 2100 \end{bmatrix}$	[0, 16, 0]
Eccentric shaft	88.1	$\begin{bmatrix} 15 & 0 & 0 \\ 0 & 1 & 0 \\ 0 & 0 & 15 \end{bmatrix}$	[0, 0, -83]

Table 3.2: Properties of the shock absorbers in the multibody model.

Attached bodies	Frame, bracket	Driving disc, drum
Number of absorbers	6	8
Item # in Figure 3.2	22	10
Normal stiffness [N/m]	1 750 000	1 400 000
Tangential stiffness [N/m]	250 000	200 000
Normal damping [kg/s]	175 000	140 000
Tangential damping [kg/s]	25 000	20 000

subcomponents. That is, the properties of the drum motor and front frame are combined to make up the mass and inertia properties of the frame rigid body. The vibration motor is combined with the bracket, and the cartridges are included in the drum. The steering hitch mass is included in the frame rigid body. The inertia properties of each rigid body are entered as in Table 3.1. These values are extracted from machine CAD drawings. The total mass is 7340 kg, not far from the nominal weight of 7600 kg. The approximate geometries corresponding to each rigid body are shown in Figure 3.5.

The result is a three-dimensional model of the drum system, designed to capture the rigid body dynamical behaviour of the roller system. A schematic view of the multibody model with the bodies and their connections is shown in Figure 3.6. The frame is allowed to rotate around two axes. A rotational constraint is set about the y axis (pitch) on the frame, to model the steering hitch. The bracket vibrates with the drum, while the driving disc follows its rotation via springs. The only body interacting with the particles is the drum.

The shock absorbers are stiffer in the normal direction than in the tangential direction. This is realised by modelling the shock absorbers as multiaxial spring-damper elements. The positions of all springs are set according to the CAD drawings. The parameters used for the shock absorbers are presented in Table 3.2. The shock absorbers between the bracket and front frame are slightly stiffer than the ones between the drum and the driving disc.

Forward motion of $v = 1$ m/s is implemented with a PI controller that regulates horizontal driving force on the frame based on velocity feedback. The drum rotation of v/r rad/s is regulated by a P controller that applies a torque between the frame and the driving disc based on the drum angular velocity. According to Dynapac, sliding between the drum and the particles has a negative impact on the compaction performance, and the rotation of the drum on real equipment is therefore regulated to rolling without slip. Similarly, a second P controller regulates the shaft rotation with a torque from the bracket.

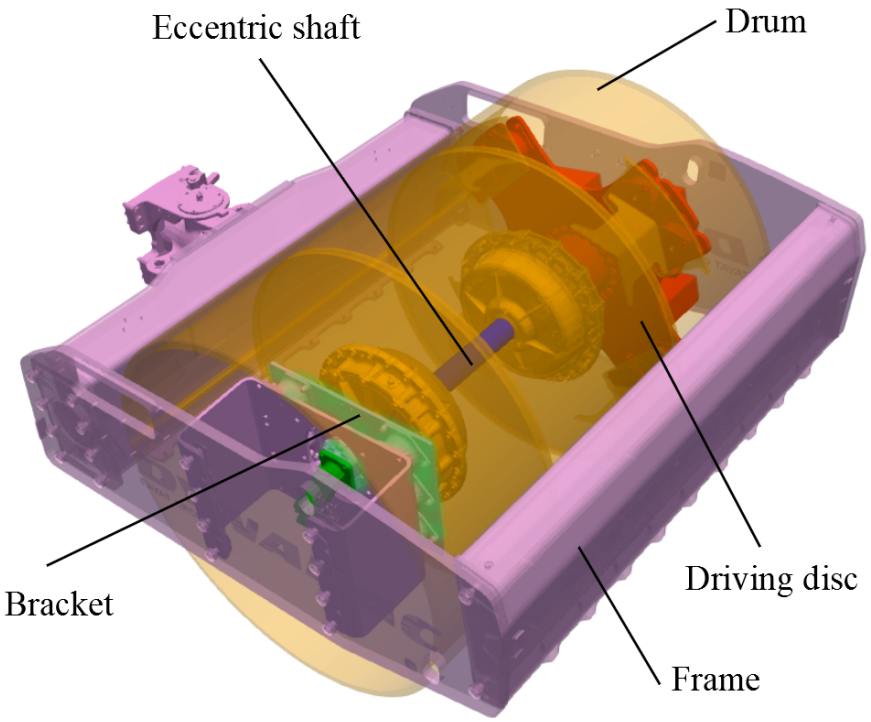

Figure 3.5: *Visualisation of the rigid bodies with their associated components.*

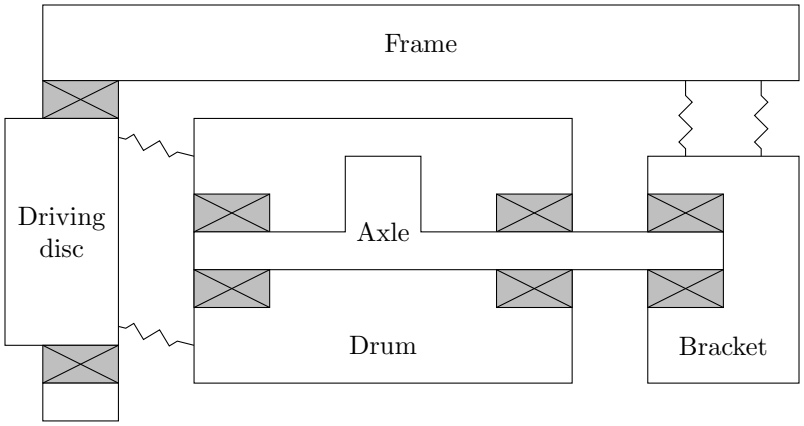

Figure 3.6: *Schematic view of the rigid body model. The system is reduced to five rigid bodies attached by springs and bearings. The bracket follows the drum translation, but does not rotate with it. The driving disc rotates, but is attached to the frame. Finally, the axle with the eccentric weights rotates independently, driven by a torque from the bracket. The force from the ground is applied to the drum, while the frame is kept upright by a constraint, modelling the steering hitch.*

4 Particle Bed Modelling

This section concerns the particle material modelling. The modelled gravel is made up of millions of particles of varying size and complex volumes and surfaces. This work uses a multisphere representation of particles, which does not capture the surface roughness exactly, but for which Hertzian contact forces can be derived. In addition, the particle bed generation method affects the bulk behaviour. Here, a method of pre-compaction up to a measured bulk density is used.

4.1 Discrete element method

Originally introduced by Cundall and Strack [8], the discrete element method models particulate matter as a system of discrete rigid particles and walls. In this software, the interaction between particles and walls is characterised by constitutive contact models in the normal and tangential directions, where the tangential forces arise due to friction. The equations of motion are integrated using a velocity Verlet algorithm [39]. The software used is Demify, developed at Fraunhofer-Chalmers Research Centre for Industrial Mathematics.

4.1.1 Contact force

This subsection describes the contact force as it is implemented in Demify. The Hertzian model combined with Mindlin's no-slip theory is implemented as presented by Thornton, Cummins, and Cleary [40]. For each pair of subspheres in contact, a normal and tangential force is calculated from the overlap. See Figure 4.1.

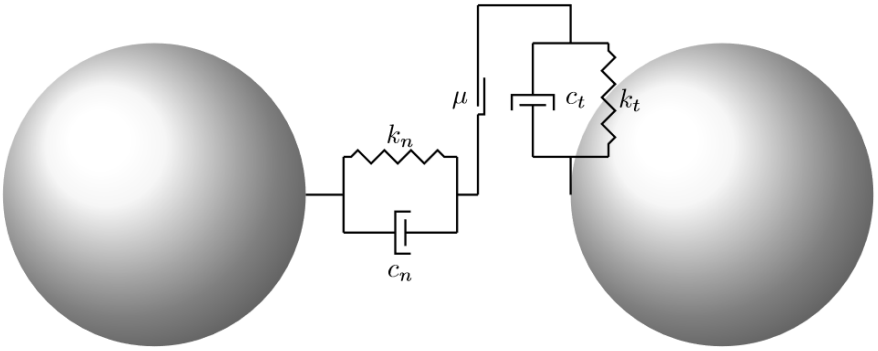

Figure 4.1: *Visualisation of the contact force model between two subspheres. Stiffnesses k_t and k_n are overlap-dependent. Damping coefficients $c = 2\gamma\sqrt{mk}$, where γ is derived from the coefficient of restitution.*

The normal force is

$$F_n = \frac{4}{3}E^\star R^{1/2}\alpha^{3/2} + 2\gamma v_n\sqrt{mk_n}, \tag{4.1}$$

where α is the relative displacement (approach), R is the effective sphere radius $R_1R_2/(R_1+R_2)$, calculated from the two subsphere radii, v_n is the relative normal surface velocity, m is the effective mass, calculated from the masses of the multisphere clumps as $m_1m_2/(m_1+m_2)$, k_n is the variable normal spring stiffness, γ is given by the coefficient of restitution e_n as

$$\gamma = \frac{-\ln e_n}{\sqrt{\pi^2 + \ln^2 e_n}}, \tag{4.2}$$

and

$$E^\star = \frac{E}{2(1-\nu^2)}, \tag{4.3}$$

where E is Young's modulus and ν is Poisson's ratio.

The tangential force at the time t^n in timestep n is increased with the tangential displacement increment $\Delta\delta^n$ multiplied by a stiffness k_t. Further, the tangential force response differs between loading and unloading,

as determined by the increment ΔF_n^n of the normal force. The elastic component F_{te}^n of the tangential force is

$$F_{te}^n = \begin{cases} F_{te}^{n-1} + k_t^n \Delta\delta^n & \text{if} \quad \Delta F_n^n \geq 0 \\ F_{te}^{n-1} \left(\frac{k_t^n}{k_t^{n-1}} \right) + k_t^n \Delta\delta^n & \text{if} \quad \Delta F_n^n < 0 \end{cases}, \tag{4.4}$$

Finally, there is an upper limit of the possible tangential force given by the interface friction coefficient μ. The tangential force F_t^n is calculated as

$$F_t^n = \min\{F_{te}^n + 2\gamma v_t \sqrt{m k_t},\ \mu F_n^n\}. \tag{4.5}$$

Normal and tangential spring stiffnesses are given by

$$k_n = 2E^\star \sqrt{R\alpha}, \quad k_t = 8G^\star \sqrt{R\alpha}. \tag{4.6}$$

$G^\star$ is related to the shear modulus G by

$$G^\star = \frac{G}{2(2-\nu)}. \tag{4.7}$$

4.2 Multisphere model and size distribution

In the model used here, the particles are modelled as clumps. A clump, or multisphere, comprises a number of overlapping subspheres. It is rigid, which means that the subspheres remain at a fixed relative distance and do not act with any contact forces on each other. The mass and inertia tensor of the clump are based on the volume occupied by the subspheres, which means that the mechanical properties of the clump are not the sum of those of its subspheres. Compared to spherical particles, clumps have the potential to capture more complex physics such as interlocking between particles, as well as more realistic rotations and friction [41]. Because of its effects on the bulk shear resistance, interlocking is expected to be especially important when modelling compaction.

With the multisphere approach, it is assumed that the sum of the forces in all subsphere contacts is a valid model of the contact force between real particles. Whether or not this is the case, and whether the contact force converges with more subspheres, is a well-known problem in the literature (e.g. Kruggel-Emden et al. [42]). The calibration performed in Chapter 6 examines the effects of this problem to an extent.

The clumps are based on the geometry of ten scanned real gravel particles. The subspheres are distributed in the clump with the shape optimising algorithm available in Demify. This process is repeated automatically for each number of subspheres n_{sph}. Next, clumps are scaled to characteristic lengths determined by the size distribution in each case. The measure of characteristic length is determined as the second largest dimension of the bounding box containing the clump. This corresponds roughly to the characteristic dimension as measured in a sieve analysis.

The material used in the experiments is a non-standard 8/90 fraction. Standard sieve analysis will be performed within the Digiroad project, but since no such measurements were yet available at the time of simulations, particle sizes are based on specifications given in CE product sheets on particle distribution of gravel from Vambåsa, Sweden [43]. The product specification is for 0/90 material, but simply removing the material below 8 mm results in the 8/90 distribution shown in Figure 4.3. For simplicity, it is implemented as a log-uniform distribution. The particle fraction to be simulated is split into ten intervals equally spaced on a logarithmic scale, where the mass of particles in each interval is set to make up 10 % of the total mass. Since more small particles are needed to make up a given mass, this means that the vast majority of the number of particles are small.

There is a computational cost associated with increasing the number of subspheres and decreasing the smallest particle size. This cost stems from two factors. Of course, there are more spheres to handle for the contact search algorithm and memory. In addition, smaller subspheres are subject to a larger overlap relative to their size, which makes the method more sensitive to instability. This must be countered with a reduced timestep, which also increases the computational effort. Therefore, the computational resources put a limit on the smallest possible particle size, which is problematic given the importance of correct size distribution. One way of alleviating this problem is to apply a resolution method. It is assumed that the surface properties of large particles are more important than those of small particles. Therefore, the number of subspheres is varied to save computational time. The larger the particle, the more subspheres are assigned to its clump. This

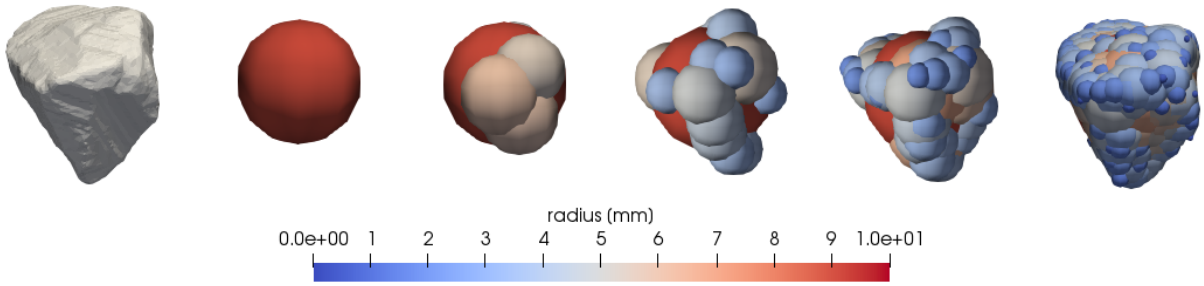

Figure 4.2: *The leftmost particle is a triangulation generated by 3D scanning of a real gravel particle, followed by multisphere representations of 1, 6, 20, 60, and 200 subspheres. Note that the shape optimisation is performed primarily to mimic the surface and not the volume of the scanned particle. At generation, the clumps are scaled to the correct particle size.*

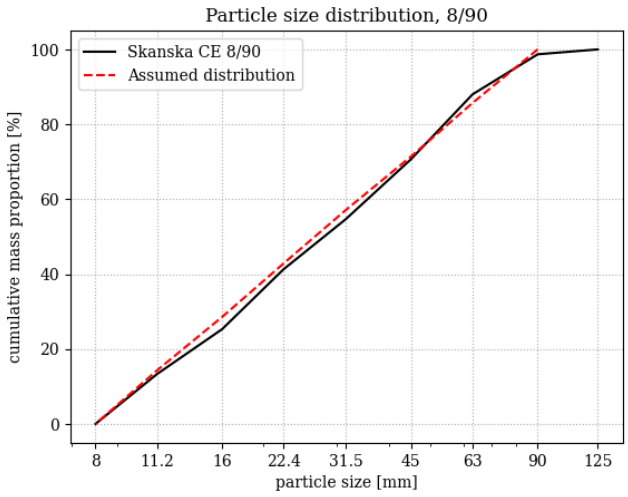

Figure 4.3: *Particle size distribution for 8/90 gravel from Vambåsa, taken from Skanska CE documents. A uniform distribution (red) is assumed in the simulations.*

resolution method is another built-in feature of Demify. Since most particles are small, the average number of subspheres is close to the number in the smallest clump. The computational cost of adding many subspheres to large particles is therefore not great.

4.3 Bed generation method

Since the purpose is to simulate compaction – essentially the increase in bulk density of the material and how it affects the bulk mechanical properties – the choice of bed initialisation method is very important. The initial state of the bed in the experiments must be properly represented to model the bed response to vibratory compaction. The main goal of bed initialisation is to achieve a valid representation of particle size distribution, segregation, and bulk density. An incorrect representation of any of these bed properties can lead to flawed results. The bed must also be in static equilibrium. During bed initialisation, material properties can be adjusted to speed up the process. For instance, the coefficient of restitution is decreased to make the sample settle quicker by removing more kinetic energy.

Several different bed initialisation methods have been proposed. Three steps can be pinpointed in sample initialisation: placement, settling and compaction to the desired density. Peters et al. [44] placed spherical particles based on a tetrahedral mesh, and adjusted diameters and locations while keeping particles in a near-touching state. The sample was then placed under gravity loading and settled, before being compacted by a plate moving at a constant velocity. In a multisphere implementation, Stahl and Konietzky [45] instead poured particles into a cylinder from two chutes, and after settling, deleted the clumps above a certain height. Then the porosity was measured. The obtained samples were slightly more porous than in experiments but within an acceptable range.

With clumps, the kind of direct placement technique used by Peters et al. [44] may be hard to implement. In addition, it is preferable to maintain full control of the amount of mass, which would not be possible if any particles are deleted. But at the same time, the volume of the bed must be exact so that the bed depth is representative.

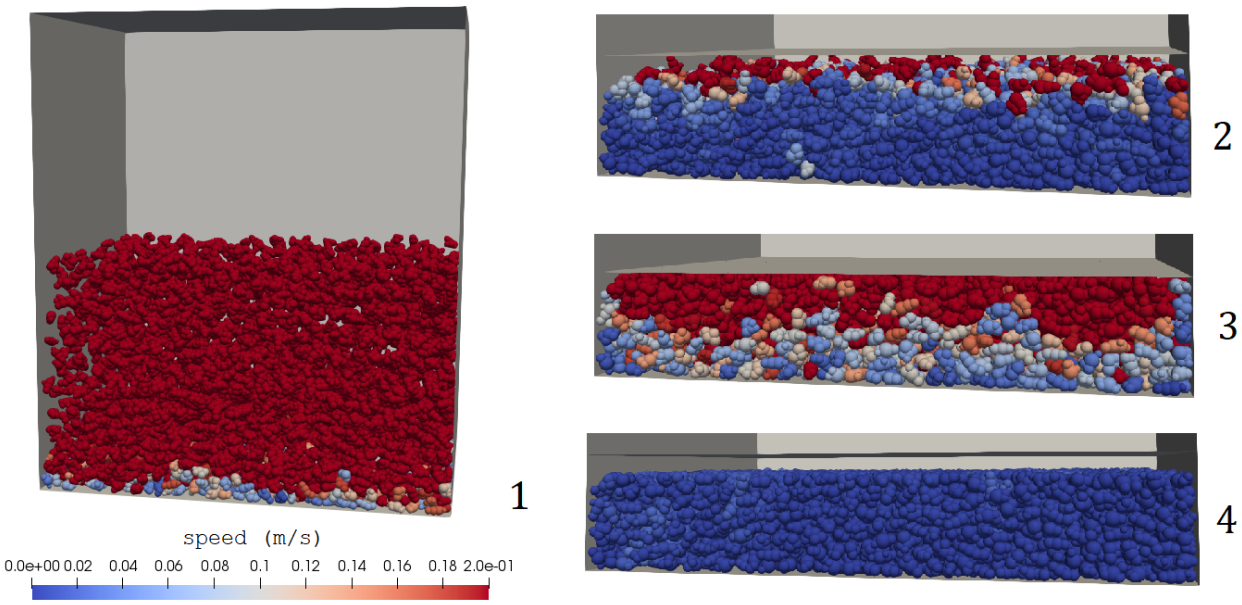

Figure 4.4: *Bed generation method. The dimensions of the desired bed are known, and particles of a mass corresponding to a given bulk density are generated as a particle rain (1). The particles are compressed to the correct height by a horizontal plate (2-3). The plate slowly retracts, leaving a flattened bed of correct bulk density (4).*

The solution used here is particle rain followed by flat compaction (Figure 4.4). Particles are generated above the channel to ensure a random distribution. After settling, the bulk volume is generally larger than desired, so a horizontal plate pushes the material from above to a box-shape of given volume. The particles

are left to settle while the plate slowly retracts. Since mass is maintained, the bulk density can be controlled by varying the mass for a given box volume. In addition, a flat surface of the bed is achieved, which ensures smooth roller movement. The box dimensions are set to mimic the dimensions of the concrete channel used in experiments, and the mass is adjusted to achieve the measured bulk density.

The beds are generated separate from the compaction simulation. The generated beds are subsequently imported and reused for various compaction cases. The advantage of bed import is saved computational effort, with reusable results, shorter simulations, and the ability to adjust the timestep and other parameters for the bed generation specifically. The drawback is a loss in statistical realisation. If the bed properties vary between generations, this variation is not captured with one reused bed. In this case, computational effort is prioritised, under the assumption that the number of particles is large enough not to result in large variation in the bulk behaviour.

5 Coupling of the Multibody Solver to DEM

The objective of this chapter is to establish an algorithm that allows for simultaneous solution of a multibody system and the discrete element problem. In such a co-simulation, the solvers operate with different timesteps, and velocity and load data is transferred between the solvers at a high frequency. Here, the methods are selected based on the requirements of the application. The focus is on developing a working model with acceptable error limits, rather than maximising performance. An algorithm is described, that solves the Newton-Euler equations at sufficient accuracy. Furthermore, the implementation of the roller model is verified, and timestep convergence is demonstrated. Finally, a DEM-MBS co-simulation framework is designed, and the method is verified with a coupled pendulum case.

5.1 System solution and algorithm

For the multibody solver, an explicit integration scheme is applied. This assumes that the right-hand side of Equation 3.13 remains constant in each timestep. The method introduces growing errors in the movement and constraints, but since simulations will only last a few seconds, sufficiently fine time-discretisation can reduce the errors to a negligible level.

The algorithm for an explicit Euler approach that simulates the time interval $t \in [0, T]$ with timestep Δt is laid out in Figure 5.1. This solution scheme requires a small timestep to assure stability and acceptable errors. Since the associated computational effort compared to DEM is expected to be negligible, simplicity is prioritised over speed in the MBS. This is also the motivation behind the choice of explicit integration.

First, the user inputs a number of bodies with mass and inertia properties, and assigns constraints and loads between the bodies at defined points. Then, the bodies are positioned so that all constraints are fulfilled. The mass matrix is assembled from the inertia properties of each body, and the external force vector is calculated and assembled. Next, the Jacobian is assembled along with the constraint force vector. The system is solved and the velocities updated. The updated velocities are then used to calculate the new body positions, and the transformation from vector rotations to quaternions is performed. Finally, the mass matrix is again assembled and the process is repeated until a specified time limit is reached.

5.2 Verification of the roller model

A plane model of the drum system is obtained if the frame is fixed, gravity is neglected, and the drum motion is studied as the eccentric shaft rotates. The rotation of the shaft can be regarded as a rotating force acting on the drum, which starts to oscillate. It translates in the $x-z$ plane in a circular motion, with the same frequency as the shaft and an amplitude A, which can be derived from the equations of motion with the following model, provided by Dynapac. Starting with

$$\begin{aligned} mr_o\omega^2\cos(\omega t) - kx &= M\ddot{x}, \\ mr_o\omega^2\sin(\omega t) - kz &= M\ddot{z}, \end{aligned} \tag{5.1}$$

where m is the mass of the eccentric weight, r_o is the distance of its mass centre from the axis of rotation of the drum, ω is its angular velocity, k is the sum of stiffnesses of the springs suspending the drum, and M is the mass of the drum and other suspended components. Using the ansatz $z = A\sin(\omega t)$ and differentiating twice yields

$$A = \frac{mr_o\omega^2}{k - M\omega^2}. \tag{5.2}$$

The same amplitude is obtained in the x direction. Note that when k is small relative to $M\omega^2$, the amplitude is negative. The drum then oscillates with a displacement opposite to the eccentric weight, as shown in Figure 5.2.

The roller model is tested in the multibody solver by removing all gravitational forces and fixing the frame to the ground. The eccentric shaft is given an initial angular velocity corresponding to 29 Hz, and damping is disabled. In the absence of damping, transient effects are avoided by choosing proper starting conditions. The drum is initially displaced by the expected amplitude and given a velocity that corresponds to the expected

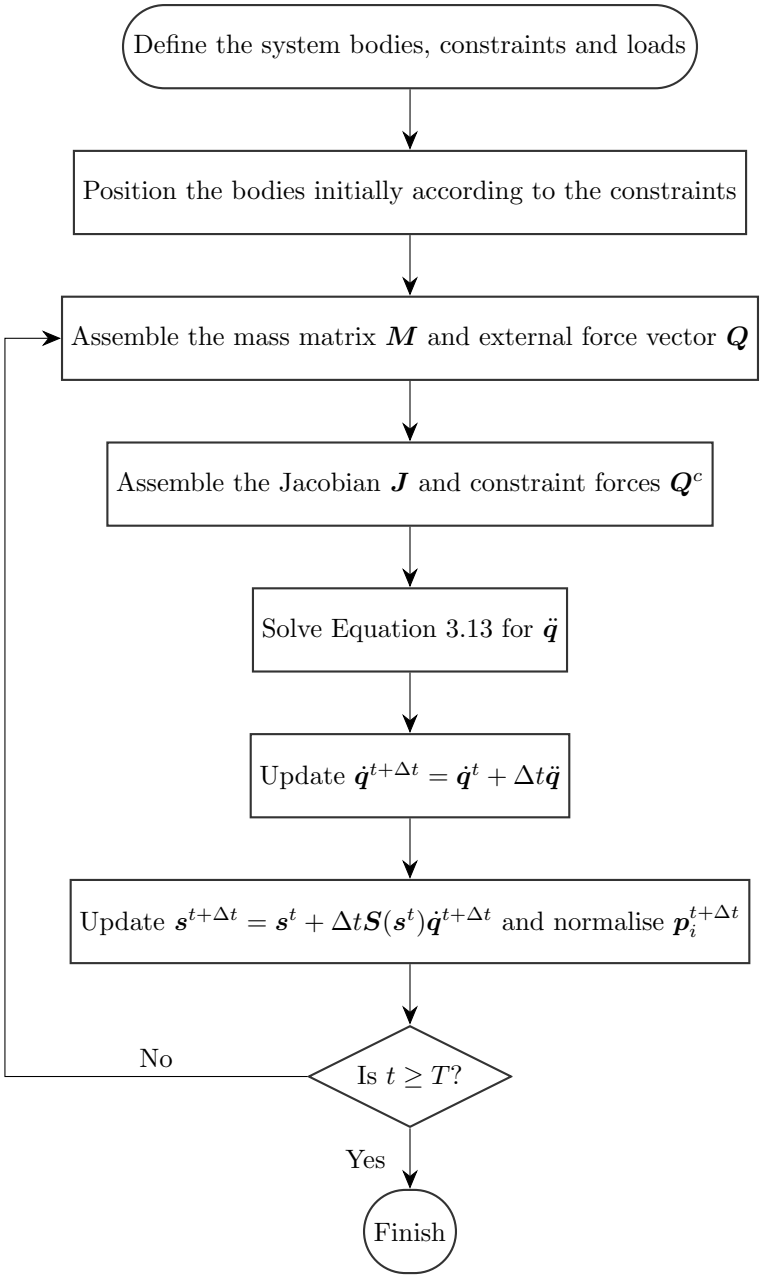

Figure 5.1: *Flowchart for the algorithm implemented in the multibody solver.*

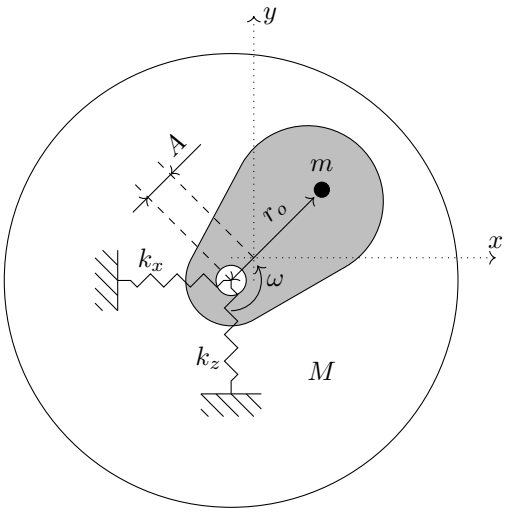

Figure 5.2: *If the frame is fixed to the ground, the amplitude A of drum oscillations can be derived, given an eccentricity* ωr_o.

dynamic equilibrium. The appropriate initial velocities, directly derived from the equations of motion, are

$$\begin{aligned} V &= \frac{m r_o \omega}{M+m}, \\ v &= -\frac{M r_o \omega}{M+m}, \end{aligned} \tag{5.3}$$

where V is the velocity of the drum and bracket, and v is that of the eccentric shaft. With these initial conditions, drum oscillations with a stable amplitude given by Equation 5.2 are expected. With the masses and stiffnesses in Table 3.1 and Table 3.2, $m = 88$ kg, $M = 3874$ kg, $r_o = 0.083$ m, $k = 6 \times 250 + 8 \times 200 = 3100$ kN/m, and $\omega = 2\pi \times 29$ rad/s. The expected amplitude then amounts to

$$A = \frac{m r_o \omega^2}{k - M\omega^2} = 1.93 \text{ mm}, \tag{5.4}$$

Simulation of the corresponding 3D case in the multibody solver results in drum oscillations as shown in Figure 5.3, with a timestep of 10^{-6} s. Longer timesteps lead to larger violations of the constraints. Accumulating errors set the shaft drifting. For a timestep of 10^{-5} s, it drifts 13 mm per second vertically out of its original alignment with the drum. For our application, this is considered acceptable. If necessary, the error can be further restricted by additional reduction of the timestep, or implementation of an error correction method. Oscillations are stable, with an average amplitude of 1.9 mm and a frequency of 29 Hz. Thus, the 3D multibody model captures the oscillating behaviour of the plane roller model very well.

The limitations of the model lie in the assumption of rigidity, and the modelling of the shock absorbers. Since material elasticity is neglected, elastic vibration modes are ignored. This is not expected to affect compaction simulation which is mainly brought about by the movement of the suspended drum, but this model might be unsuitable for assessing the operator environment vibrations, for example. The shock absorbers are modelled with constant stiffness, based on the available data, which is expected to be valid at least for small displacements. The rotational stiffnesses are not modelled at all, which could have a minor effect, especially if rocking occurs, although the largest displacements are always translational. However, the main source of error is likely the risk of missing components when extracting the mechanical parameters, or an incomplete CAD drawing. The discrepancy between the measured and nominal mass described in Chapter 3 gives some estimate of this error.

5.3 Model coupling theory

Co-simulation of the discrete element method and a multibody dynamics system has the potential to simultaneously capture both material and equipment behaviour. In a DEM-MBD coupled system, contact forces from

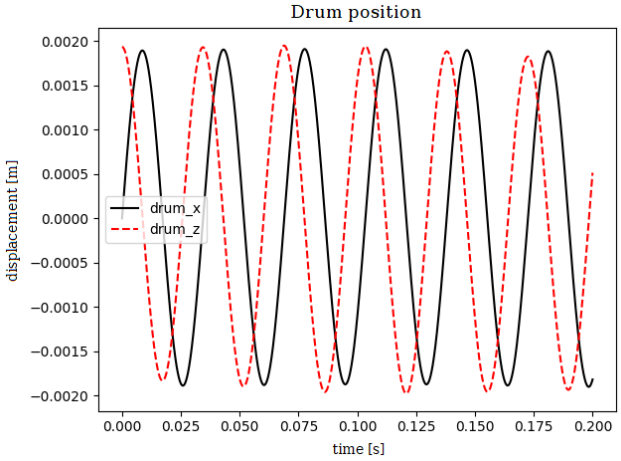

Figure 5.3: *If the frame is fixed and gravity is neglected, rotating the eccentric weights at 29 Hz excites the drum at an amplitude of approximately 1.9 mm. The corresponding value from the analytical model (Equation 5.2) is 1.93 mm.*

particles are calculated in the DEM software, and transferred to the multibody solver. The multibody solver calculates motion of the rigid bodies based on the force input, and the motion data is sent back to the DEM solver. Iteration of these steps throughout the simulation is the main framework of a co-simulation.

DEM and MBS can be regarded as two dynamical systems, which interact on each other with a contact force and moment. In particular, the multibody solver is a differential-algebraic equation system, while DEM solves particle movements as an explicit system of ordinary differential equations. The only information from DEM available to the multibody system is this single contact force, which changes depending on the movement of the drum. From the point of view of the MBS, the entire DEM system can therefore be regarded as a single highly complicated multiaxial and non-linear spring. On the other hand, in the DEM framework, the entire roller system works as a single large particle subject to an external load, i.e. the excitation and driving.

The solvers typically operate with different timesteps. DEM requires a timestep roughly on the order of 1e-6 s, while a MBD system can usually be solved around 1e-2 s. This means that between each information transfer between the solvers, considerably more timesteps will need to be solved in DEM than in MBS. A coupling server handling the exchange of data is therefore necessary [46].

In addition, the effects of the timestep ratio on the resolution of data must be checked. According to Lommen, Lodewijks, and Schott [46], a successful coupling requires (1) calculation in DEM of a resultant force on the coupled body based on its position, (2) time-averaging of the force over the multibody timestep, since several (n) DEM timesteps will have passed since the last update, (3) calculation of body positions in the MBD solver and (4) coordinate transformation of positions to the DEM coordinate system.

5.4 Implementation of a coupling server

The co-simulation algorithm is presented in Figure 5.4. This scheme alternates between simulating n timesteps in DEM, and 1 timestep in MBS, while transferring and applying the obtained forces and velocities. Instead of transferring the positions calculated by the multibody solver into DEM, the velocities are transferred and added as prescribed motions during the n DEM timesteps. This has the advantage of smoother tool movement, since the positions are updated more frequently than the velocities. Tool movement can be of considerable importance, since overlaps with stiff particles can lead to large forces. It is also less complicated to translate the angular velocity, which is a vector, than the rotational state, which is a quaternion, between the DEM and MBS coordinate systems. The drawback is that there is a possibility that body and tool positions become unaligned in the solvers if there are differences in integration. However, direct comparison of the simulation results verifies that positions and orientations agree. A future built-in MBD functionality in Demify would avoid this issue entirely.

The roller multibody system operates at a relatively high frequency of about 30 Hz. Since an explicit integration scheme is used and constraint forces are large, errors grow quickly if the multibody timestep is set

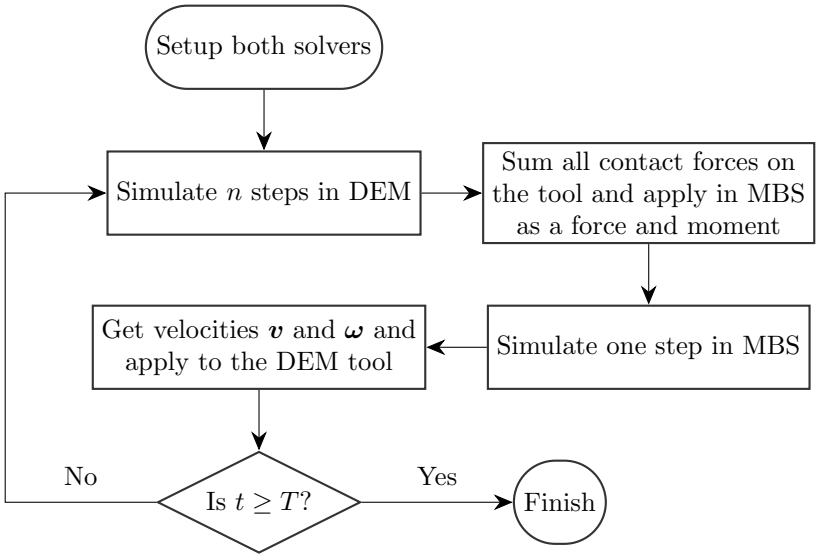

Figure 5.4: *Flowchart for the co-simulation scheme. The process alternates between the two solvers, and the results are transferred between them until a stopping criterion is met.*

too long, and constrains are violated. For a simulation of several seconds, a timestep of 10^{-5} s is found to be sufficiently small to avoid noticeable constraint violation of the eccentric shaft. This is considerably smaller than the examples put forward by Lommen, Lodewijks, and Schott [46]. The DEM timestep is on the order of 10^{-6} s. In other words, the timestep ratio n is small. Still, the computational effort spent on the multibody solver is measured as less than 1 % of that spent on DEM. This is expected, since the number of degrees of freedom in DEM is several orders of magnitude larger than in the multibody system. As n is small, force averaging is not performed, since the force variation over n timesteps is not expected to be great.

5.5 Verification of the coupled model

Since the main information provided by Demify to the multibody solver is the contact forces of particles on a rigid body object, correct forces and moments must be asserted. The tool force and moment calculations are verified by placing a number of shape-optimised multisphere cylinders at given positions on a moving plate, and extracting the contact force and moment about a given point. The total contact force in the vertical direction can then be verified by comparison to the sum of particle weights. Correct total moment is similarly checked by comparison to the sum of particle weights multiplied by distances from the moment point. The weight of the cylinders is calculated based on the volume of the multisphere discretisation and the particle material density. The force and moment on the plate are estimated at an error below 0.1 %, demonstrating correct multisphere weight and tool load calculation.

To verify the coupled movement, a pendulum case as in Figure 5.5 is set up. Around 100 multisphere particles weighing 1077 kg are loaded into a 1 m^3 cubic box. Each side of the box is coupled to a rigid body in the multibody solver, and all bodies are fixed to one another. One of the bodies is suspended at a point positioned 7 m horizontally from the centre of the box with a spherical constraint, and the box is then released under gravitational load from the particles. The ensuing oscillation can be compared to a pendulum motion, provided that the distance to the suspension point is large compared to the box size. The theoretical value for the centripetal force on a point mass of 1077 kg accelerated by gravity from any height is $2mg$. Adding the gravitational force results in $3mg \approx 31700$ N. The measured force is about 10 % higher, for several possible reasons. The filled box is not a point mass, it accumulates some rotational energy, and there may be a spring effect in the particle contact forces that gathers some energy. In addition, the centre of mass of the particles is positioned a bit below the centre of the box. Still, a comparison to the analytical case approximately verifies the implementation.

Table 5.1 presents the results of a convergence analysis of the timestep with regard to the maximum vertical force. The simulations with a MBS timestep of 10^{-4} suffered from instability and could not finish. The force is asserted to be independent of a DEM timestep lower than 10^{-5} with an error less than 1% compared to

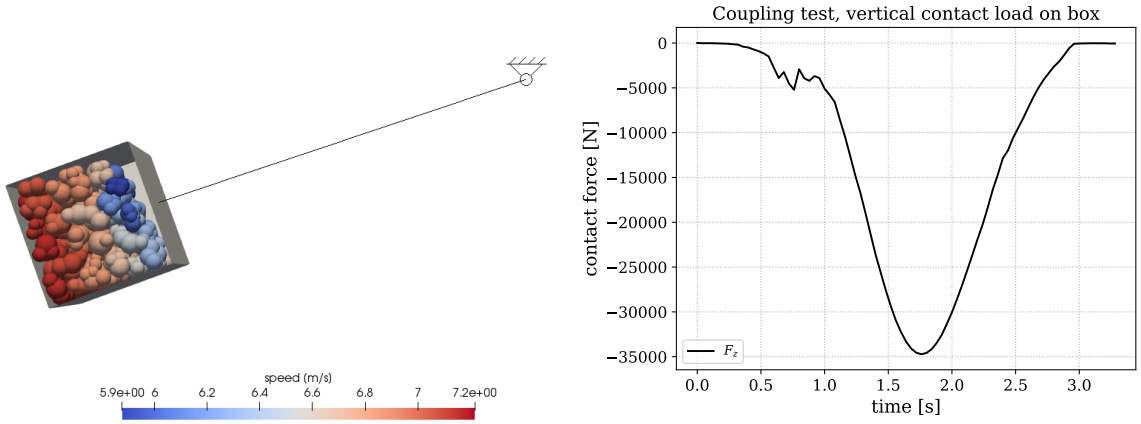

(a) (b)

Figure 5.5: *a) The setup for the coupling test. A box filled with particles is connected to a pendulum. The connection is realised with a spherical constraint in the MBS.*
b) Calculated vertical component of the sum of contact forces between box and particles. Both timesteps are 1×10^{-6}*. Note the initial load variations, which are caused by a rearrangement of the particles in the box as it starts to move.*

Table 5.1: Computed maximum vertical contact force on the box in the coupling verification test.

DEM timestep [s]	MBS timestep [s]	max force [N]
1×10^{-6}	1×10^{-6}	34724
1×10^{-6}	1×10^{-5}	34727
1×10^{-6}	1×10^{-4}	(crashed)
1×10^{-5}	1×10^{-5}	34512
1×10^{-5}	1×10^{-4}	(crashed)
3×10^{-5}	3×10^{-5}	35691

10^{-6}, and of a MBS timestep of at most 10^{-5}. Specifically, a MBS-DEM timestep ratio of 10 has a negligible effect compared to a ratio of 1, even without force averaging. It appears that the maximum force for very long timesteps (3×10^{-5}) is high because vibrations arise, probably due to large yet stable errors in DEM. In light of these observations, all subsequent coupled simulations are kept within the timestep constraints $dt_{\text{MBS}} \leq 10^{-5}$ and $dt_{\text{MBS}}/dt_{\text{DEM}} \leq 10$.

6 DEM Calibration and Compaction Experiments

This chapter presents an outline of the full-scale compaction experiments and some of their results, as well as the calibration of the DEM model. Due to the multisphere model of particle shape, calibration of contact force parameters is necessary to capture the frictional behaviour. In this chapter, a uniaxial strain test is used for the purpose of calibration.

6.1 Calibration of DEM material parameters

Calibration of the mechanical parameters is necessary to capture the bulk behaviour of the particle matter. Since irregularly shaped particles are modelled as clumps of subspheres, the particle surface will not be represented exactly. We want to determine how the discretisation of the particles influences the macroscopic frictional behaviour, and whether the coefficient of friction must be adjusted to capture it. Since there is a computational cost associated with the number of subspheres, we also want to establish how many subspheres are needed and whether the behaviour converges as the discretisation is refined. Finally, we want to establish convergence with regard to the timestep and domain size.

6.1.1 Previous work on calibration for compaction

There are many ways of calibrating parameters in DEM. Quist [47] developed a calibration framework based on design of experiments, surrogate modelling, and multiobjective optimisation. Stahl and Konietzky [45] applied no less than five tests to calibrate the friction coefficient, shear and normal stiffness of ballast and gravel. The calibration was carried out for multispheres. Of particular importance to compaction are their triaxial test, shear test, and oedometer test. Coetzee [48] also simulated an oedometer test, measuring the bulk strain as a bed of particles was subject to cyclic compressive loading and calibrating the particle stiffness after experimental results. The internal friction angle (the relation between shear stress and normal stress) was used to calibrate particle-particle friction. Peters et al. [44] simulated a mobility cone penetrometer test, where a rod with a cone-shaped tip is inserted into a bed of particles. They used spherical particles and measured porosity, particle stresses, displacements, and velocities. The porosity and initial stress had a major influence on the cone resistance, which shows the importance of proper bed initialisation. Genetic algorithms can also be used for parameter calibration and optimising computational effort [49]. Rackl and Hanley [50] used Latin hypercube sampling combined with Kriging as a methodical calibration approach. They used the angle of repose and the bulk density as responses.

For our implementation, the compaction behaviour of the material is considerably more important than the flow behaviour. The macroscopic behaviour that must be captured includes the bulk density, the stress-strain relation in axial compression and the shear behaviour resulting from interparticular friction. The primary parameters to calibrate are coefficient of friction μ, Young's modulus E, and the particle discretisation. The discretisation is part of the calibration because of the interplay of the coefficient of friction and the number of subspheres in the clump. An increase in the number of subspheres leads to a more rugged surface, which may affect the value of μ necessary to successfully capture the shear behaviour. In other words, in a multisphere method, unlike in continuum methods, simply refining the discretisation does not necessarily lead to a converging error.

6.1.2 Uniaxial strain test

In the uniaxial strain test, a rigid cylinder is filled with particles, which are compressed from above by a horizontal plate. Here, some of the data from the uniaxial strain test experiments performed in "WP3 - Laboratory compaction experiments" of Digiroad is used for calibration of DEM material parameters. In order to make the simulations as fast as possible and enable more realisations, the experimental data-set with the coarsest particles is selected. The particle size distribution in the experiments is based on the Fuller equation [51],

$$p(d) = \left(\frac{d}{d_{\max}} \right)^n, \tag{6.1}$$

where $p(d)$ is the cumulative passing up to particle size d, $d_{\max}$ is the upper particle size limit, and n is the parameter characterising the distribution. The selected data-set is for a distribution with an exponent $n = 5$ in

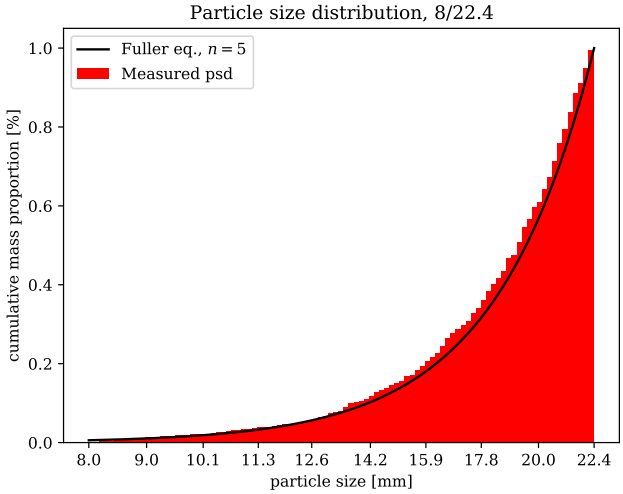

Figure 6.1: *The measured particle size distribution in the uniaxial strain test. The distribution is defined by the Fuller equation with an exponent $n = 5$.*

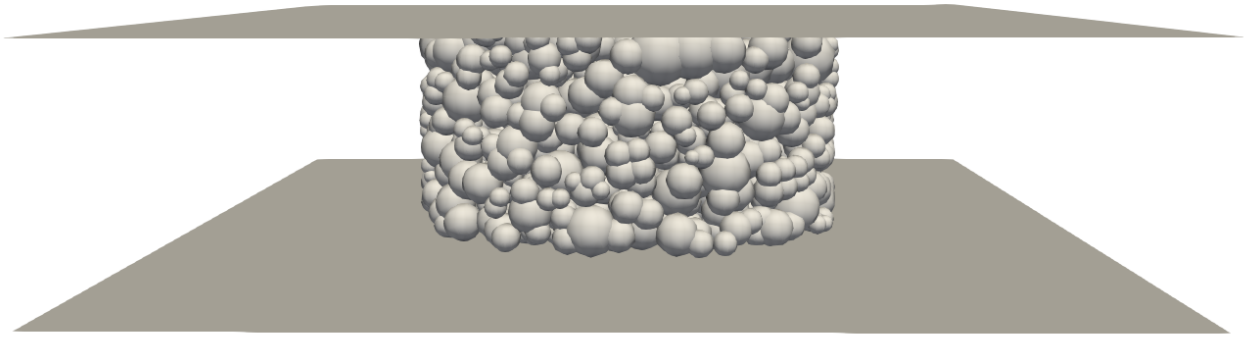

Figure 6.2: *Schematic configuration of the uniaxial strain numerical test. The material is compressed by the top plate and the stress-strain relation is measured. The rigid cylinder wall is not shown here.*

the size range up to 22.4 mm. The same distribution is applied in DEM. The implementation of the Fuller equation is verified by measurement of the size distribution among the generated particles, shown in Figure 6.1.

The cylinder has a diameter of 170 mm and a height of 90 mm. The material is compacted with a pulsating load of 250 kPa. Before application of the cyclic load, the material is pre-compacted at 88 kPa.

The rig is modelled as a particle-filled cylinder, as shown in Figure 6.2. 2.75 kg of material is generated by particle rain into the cylinder. The size range is limited to 8/22.4 to simplify computations, since particles smaller than 8 mm make up less than 1 % of the total mass. The material is pre-compacted as in the experiments. The plate movement is controlled with a P regulator, limited to 1 mm/s, to ensure quasi-static conditions. The goal function is the average stress-strain relationship as recorded in the experiments, in particular the average strain observed at 250 kPa. The primary material parameters to be calibrated are the Young's modulus E, the coefficient of friction μ, and the set of subsphere configurations used to generate the clumps. Since particle movement is slow, the influence of the coefficient of restitution is expected to be small, and, consequently, it is fixed at 0.8, typical for granite balls [52]. This value is used throughout the project for the coefficient of restitution. The generalisation of this parameter from a sphere to a multisphere is not evident, but the value is verified not to play a major role for results. A typical natural range of Young's modulus for granite is $[10, 50]$ GPa, with even lower values for very altered samples [53].

A number of different clump sets and parameter combinations are numerically evaluated. In order to save computational effort, all parameter combinations are not tested. Rather, a number of candidate solutions based on typical parameter values are first tested, and their parameters are then modified according to how

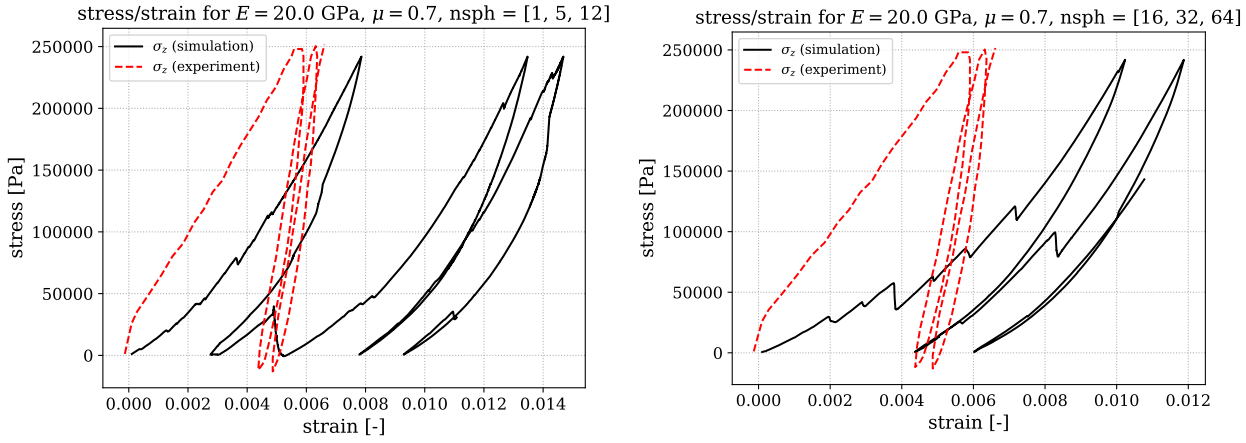

(a) (b)

Figure 6.3: *Stress-strain results for two realisations of the numerical uniaxial strain test, with $E = 20$ GPa, $\mu = 0.7$. a) Clumps with $\{1, 5, 12\}$ subspheres. b) Clumps with $\{16, 32, 64\}$ subspheres. Just as in the experiments, the first cycle is less stiff than the subsequent load response.*

the total strain of the first load cycle compares to the average experimental result. Adjustments are made under the assumption that increasing E or μ should increase the bulk stiffness of the material. The total number of successfully completed simulations is 20. In these simulations, parameters are varied in the ranges $E \in [20, 160]$ GPa and $\mu \in [0.4, 2.2]$. A value of $\mu > 1$ has no clear physical interpretation, but higher values are tested to assess the effect of friction in a broader scope. The five tested subsphere configurations are $n_{\text{sph}} \in \{2, 4\}, \{1, 5, 12\}, \{4, 8, 16\}, \{8, 16, 32\}, \{16, 32, 64\}$.

A large variance in the measured strain is observed, due to unpredictable avalanche events, as the force chains collapse when the friction condition is superseded at some contact. These stress drops lead to a rearrangement of the particle bed to a denser state. Two representative examples of stress-strain curves for different clump sets are shown in Figure 6.3. Stress drops are visible, as is the non-linearity of the elasticity.

The parameter combination that resembled the stress-strain curve from experiments closest in terms of the maximal strain in the first cycle is $E = 160$ GPa, $\mu = 0.7$, with 4, 8, and 16 subspheres. The stress-strain relation for this parameter set is compared to the average experimental values in Figure 6.4. This figure shows that there is a qualitative discrepancy in the shape of the stress-strain curve between experiments and simulation. In the experiments, the relation under loading is almost linear, but in the simulations, there seems to be a power relation. This likely stems from the Hertzian formulation of the contact force in Equation 4.6, with the exponent 1.5 for the subsphere overlap. Further, no stress drops occur in the experiment. Finally, hysteresis loops are observed in the experiment, but not in the simulations. These qualitative discrepancies show that there is a limit to what calibration of the selected parameters can achieve in terms of capturing the behaviour from experiments.

Interestingly, the number of subspheres had no clear correlation with the bulk stiffness of the material. The subsphere configuration may have a larger impact on the shear strength of the material, however.

The gradient of the stress with regard to the strain is of interest, because unlike strain measurements, it is unaffected by stress drops. Numerical differentiation shows that the gradient does not increase by much when the Young's modulus is increased. This is tested with measurement of the gradient the first time the stress supersedes 200 kPa, a value selected because it has few occurrences of stress drops in all simulations. Four realisations of the same case ($E = 160$ GPa, $\mu = 0.7$, $n_{\text{sph}} \in \{4, 8, 16\}$) results in an average gradient of 81.9 MPa with a sample standard deviation of 16.2 MPa. A single test with the same parameters but with E changed to 20 GPa results in a gradient of 61.0 MPa. The gradient decreases slightly with E, but given the variance of the tests and the low number of realisations, the difference is not statistically significant.

For the coefficient of friction, there is no measurable change in the gradient at 200 kPa for a given value of E. One explanation would be that the gradient is dominated by the normal component of the contact force, with no effect from the tangential component. This is in line with the observation that the stress-strain curve is non-linear, since, unlike the tangential force, the normal force expression has an exponent 1.5 for the subsphere

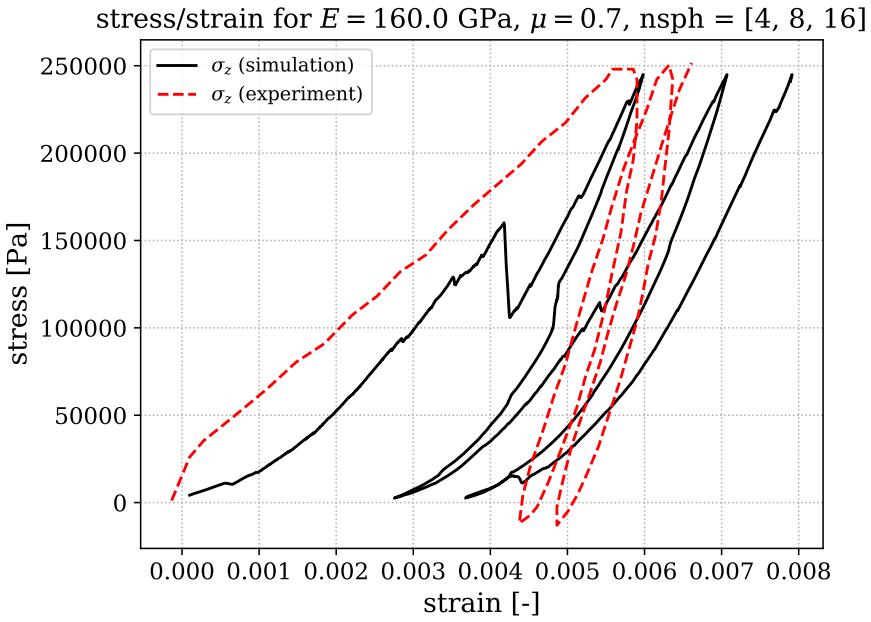

Figure 6.4: *Best fit to experimental results of all tested parameter combinations for the uniaxial strain test.*

overlap factor.

Overall, it has been shown that under the tested conditions, very little change in the angle of the stress-strain curve can be achieved by calibration of E, μ, and n_{sph}. E possibly has a small effect, while no effect has been observed for the other two parameters. However, aside from the gradient, the observed bulk stiffness is also affected by the number and magnitude of stress drops. It could be possible to calibrate the stress drops so that the bulk stiffness would be approximately right; in fact, Figure 6.4 is an example of this. However, a problem with this approach is that there is no clear equivalent to the stress drops in the experimental results.

Finally, it should be noted that previous experience indicates that rearrangements of particle beds are sensitive to the time step, due to the fast alterations of contact forces. These tests are run with a timestep of 10^{-6}, which may be too long. On the other hand, with a shorter timestep, fewer realisations than 20 would be possible. Still, a convergence study with regard to the timestep shows that a timestep reduction can reduce the magnitude and number of stress drops. The gradient of the stress-strain relation does not change, however.

6.2 Compaction experiments setup

Full-scale compaction experiments are part of the Vinnova InfraSweden2030 DigiRoad project, "WP4 - Full-scale experiments". Experiments are conducted with the cooperation of Dynapac AB, and also supported by SBUF project 13820. Since these experiments are part of a different project, and since complete results are yet to be published, a full description is outside the scope of this thesis. An overview is given in this section, with a subset of results relevant to this thesis. Further details of the experiments can be found in the project application, [14].

12 passages with a Dynapac CA3500D vibratory roller (Figure 3.1) are performed over a particle bed consisting of three segments of different size distributions and depths. Load cells are placed inside the particle bed at a depth of 0.5 m and 1 m, as shown in Figure 6.5. 3D scanning is performed before and after compaction to measure the volume change of the bed. Before the start of the experiments, the roller passes twice over the material without any vibration. In the simulations, this is represented by the bed initialisation scheme.

The material is granite, taken from Vambåsa, Blekinge in Sweden. The material and bed specifications of the three segments are shown in Table 6.1. The material is distributed by an excavator to minimise segregation. The bulk density is measured on-site by filling a box of $367 \times 270 \times 225$ mm with material and weighing the contents. Three measurements are made for each particle size fraction.

The solid density had previously been measured on 11 sampled rocks, prepared by washing, cleaning, oven-drying, and weighing in air and in water. The resulting average density from that analysis was 2645

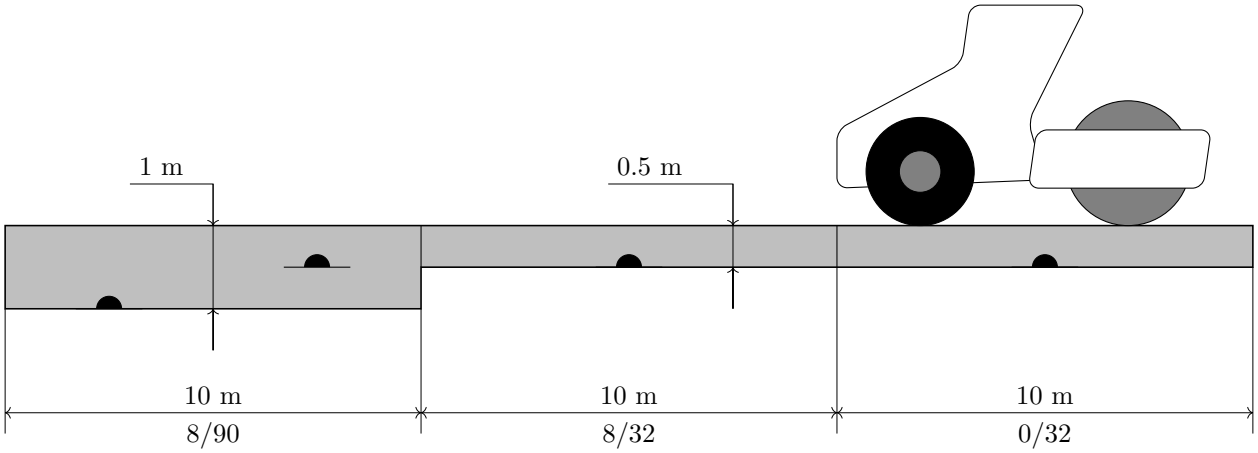

Figure 6.5: *The experiment setup. The load cells, marked by half circles, are placed at 0.5 m and 1.0 m depth according to the figure. Figure not to scale.*

Figure 6.6: *The experiment setup before and after filling. The load cells are positioned at the bottom of the channel, and granular material is placed on top with an excavator.*

kg/m^3, with a standard deviation of 16.6 kg/m^3.

Table 6.1: During the experiments, three material beds are compacted. Three different particle size fractions and two bed depths are tested.

particle size fraction [mm]	0/32	8/32	8/90
bed depth [m]	0.5	0.5	1.0
bulk density avg. [kg/m]	1501.7	1381.7	1476.6
bulk density std. dev. [kg/m]	8.80	6.06	32.87
avg. compaction degree [%]	56.8	52.2	55.8

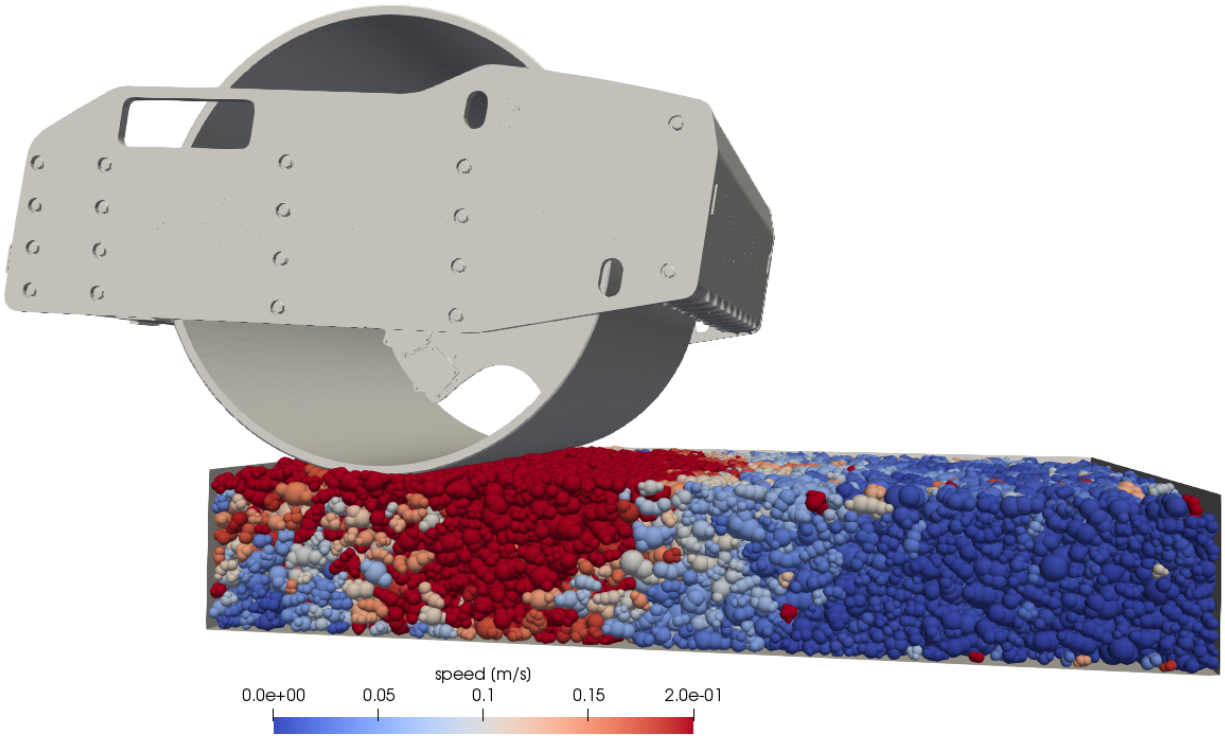

Figure 7.1: *First impact against a* $3 \times 2.5 \times 0.5$ *m bed with a particle fraction of 45/120 mm. The colouring according to velocity magnitude gives an impression of how forces spread within the bed – downwards and forwards.*

7 Compaction Simulation Results

This chapter presents the results of the coupled MBS-DEM simulation of compaction. Comparison of simulation and experimental bed stress measurements shows qualitative agreement, but the simulated compaction profile is unrealistic. The simulated drum response is also examined, and compared to the compaction theory of Chapter 2. Figure 7.1 shows a representative result: a simulated 45/120 bed at the start of compaction. The spread of kinetic energy into the bed is apparent when particles are coloured according to speed.

7.1 Simulation assumptions

Beds of varying particle size distributions, depths, clump sets, and material properties are compacted. Further parameter values are listed in Table 7.1. Since the calibration results were inconclusive, compaction of three different particle Young's moduli are tested. This also enables study of the machine response to beds with material of varying stiffness. Early testing indicated that lower values resulted in more realistic results. Based on this experience, and typical values for granite [53], the values of E are selected in the range of $[1, 20]$ GPa. The parameters for the roller material are set to typical steel values. This material is also used for the walls.

The width of the material bed, 2.5 m, gives a distance to the wall of 185 mm, which gives enough room for particles to be squeezed out on the sides of the roller. Tests show that a shorter distance has an impact on the shear strength and penetration, and that 2.5 m provides an acceptable balance between computational cost and unwanted boundary effects. In the experiments, this distance was about 600 mm on one side, and several meters on the other.

Since the compaction degree after the static passage in the experiments was unknown at the time of the simulations, the bulk density for the uncompacted 8/90 bed is used, as measured in Table 6.1. This is too porous, but test simulations of slightly higher initial compaction degree indicate no significant effect on results.

Table 7.1: List of parameters. These values are the same for all compaction simulations. ν is based on [54].

Description	Symbol	Value
Coefficient of restitution	e	0.8
Bed length	l_x	3000 mm
Bed width	l_y	2500 mm
Particle density	ρ	2640 kg/m^3
Poisson's ratio	ν	0.17
Roller radius	R_r	759 mm
Roller velocity	v_r	1 m/s
Roller-particle friction	μ_rp	0.2

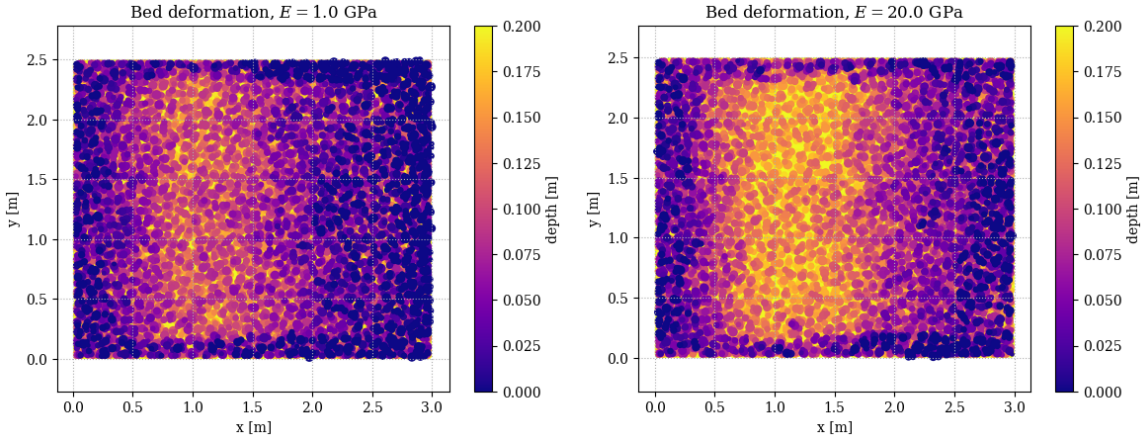

Figure 7.2: *Heat maps of the bed height after compaction, as seen from above, with varying Young's modulus. Left: $E = 1$ GPa. Right: $E = 20$ GPa. In both cases, a clear track is visible in the roller path. A larger deformation is visible in the bed of stiffer material.*

The drum is initialised 10 mm above the bed, and then slowly lowered into the particle bed, until the contact forces equal the gravitational force of the front module. This is made so as not to damage the bed structure unnecessarily at the first impact.

7.2 Bed displacement profile

After roll-over, particle positions are extracted to give a measure of bed deformation and compaction. Then, the bed surface is divided into a grid of padded rectangles. A heat map is constructed from the z position of the top of the most elevated particle in each rectangle. Averaging the values of the heat map gives an estimate of the overall compaction.

Heat maps of $3 \times 2.5 \times 0.5$ beds of different Young's moduli, compacted with 29 Hz vibration, are shown in Figure 7.2. The beds consist of monodisperse 90 mm particles with 4 subspheres. The drum, which has rolled over the bed from left to right in these figures, clearly leaves a suppressed track. The degree of compaction is larger for the stiffer bed.

In order to study the side profile of the middle of the bed, particles within one half particle length of the centre-line of the bed are plotted. The beds from Figure 7.2 are shown in profile in Figure 7.3. The compacted profile is arc-shaped, since the shear strength of the material is increased by the proximity to the walls. The profile is also non-symmetric. This is because the drum first digs into the bed and then slowly ascends as it moves forward, primarily due to the material that builds up in front of the drum and eventually forces it upwards.

The velocity field during compaction is shown in Figure 7.4. As is suggested in the series of pictures, a considerable number of particles are pushed ahead of the roller and over the bed wall to the right in the figures. On average, about 5 % of the particle mass is pushed outside the initial box. We also get a perception of the direction of compaction forces. The drum mainly affects the volume below and ahead of its contact point, and

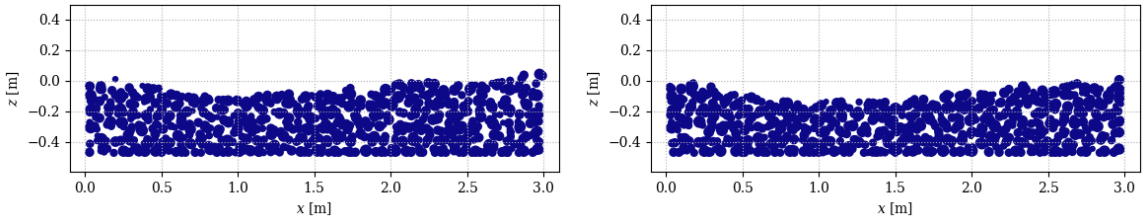

Figure 7.3: *Bed centre profiles after compaction of monodisperse particles. Left: $E = 1$ GPa. Right: $E = 20$ GPa. The subspheres whose centre points lie within one half particle diameter of the xz half-plane of the bed are shown. This gives an impression of the porosity of the bed.*

Table 7.2: Bed compaction results. A reduction in average bed height is achieved in all cases. However, the bulk density does not always go up, as material is also pushed off the bed by the roller. The initial bulk density is on average 1470 kg/m^3. The density ratio shows the actually performed increase in bulk density.

E [GPa]	n_{sph}	fraction [mm]	depth [mm]	avg. Δh [mm]	bulk density [kg/m^3]	density ratio
1	4	90/90	500	-47.7	1445	0.982
10	4	90/90	500	-80.5	1487	1.01
20	4	90/90	500	-86.5	1489	1.01
1	4	90/90	1000	-59.6	1516	1.03
20	{4,8}	45/120	500	-127	1431	0.957
20	10	90/90	500	-34.7	1438	0.967

there are shock waves spreading throughout the bed in all directions.

The results of the heat map average bed heights are shown in Table 7.2. The average height is compared before and after compaction. The mass of the compacted part of the bed is measured by excluding particles within 0.5 m of the vertical walls, to reduce the influence of the boundaries. From this mass and the average height, the bulk density is calculated. The initial bulk density varies slightly between runs due to different beds, and therefore Table 7.2 also shows the ratio of the resulting and initial bulk densities. A value above 1 indicates that some compaction of the bed has been achieved.

Although the height decreases in all simulations, the cause is not primarily compaction, but rather material that is pushed in front of the roller and over the edge of the bed, as well as to the sides of the roller. This results in a loss of mass in the domain, which is why the bulk density must be studied in addition to the bed height. In most cases, about 6-9 % of mass is pushed off the bed entirely. The most extreme case is that of 45/120, where 12 % of the material is pushed outside the bed box, resulting in the large height change of -127 mm, while still leaving the bed less compacted than at the offset. The cause of excessive material pushing compared to experiments appears to be insufficient shear resistance, which makes the roller sink into the bed and plough the material ahead. The data suggest that this shear resistance is particularly weak for slightly wider fractions. The relation between density and particle size distribution is a geometric phenomenon, and it is possible that an even wider fraction would again result in a higher resistance, since small particles fitting in between large ones can increase the maximal potential bulk density. Finally, it can be noted that an increase in the number of subspheres resulted in a more realistic height change, i.e. a better shear resistance, although actual compaction of the material still is not performed. Probably, much more subspheres than 10 are needed to create a contact skeleton that is strong enough to sustain realistic deformation.

7.3 Load cell response

Throughout compaction simulations, the vertical load on a square section of the channel floor is measured, as shown in Figure 7.5. This section measures 204×204 mm, giving an area equivalent to that of the round load cell used in the experiments. Dividing the load with the area gives an average stress at the bottom of the bed, comparable to the stresses measured in the experiments.

As the vibrating roller passes above the sensor, the measured stresses come in spikes that first increase and

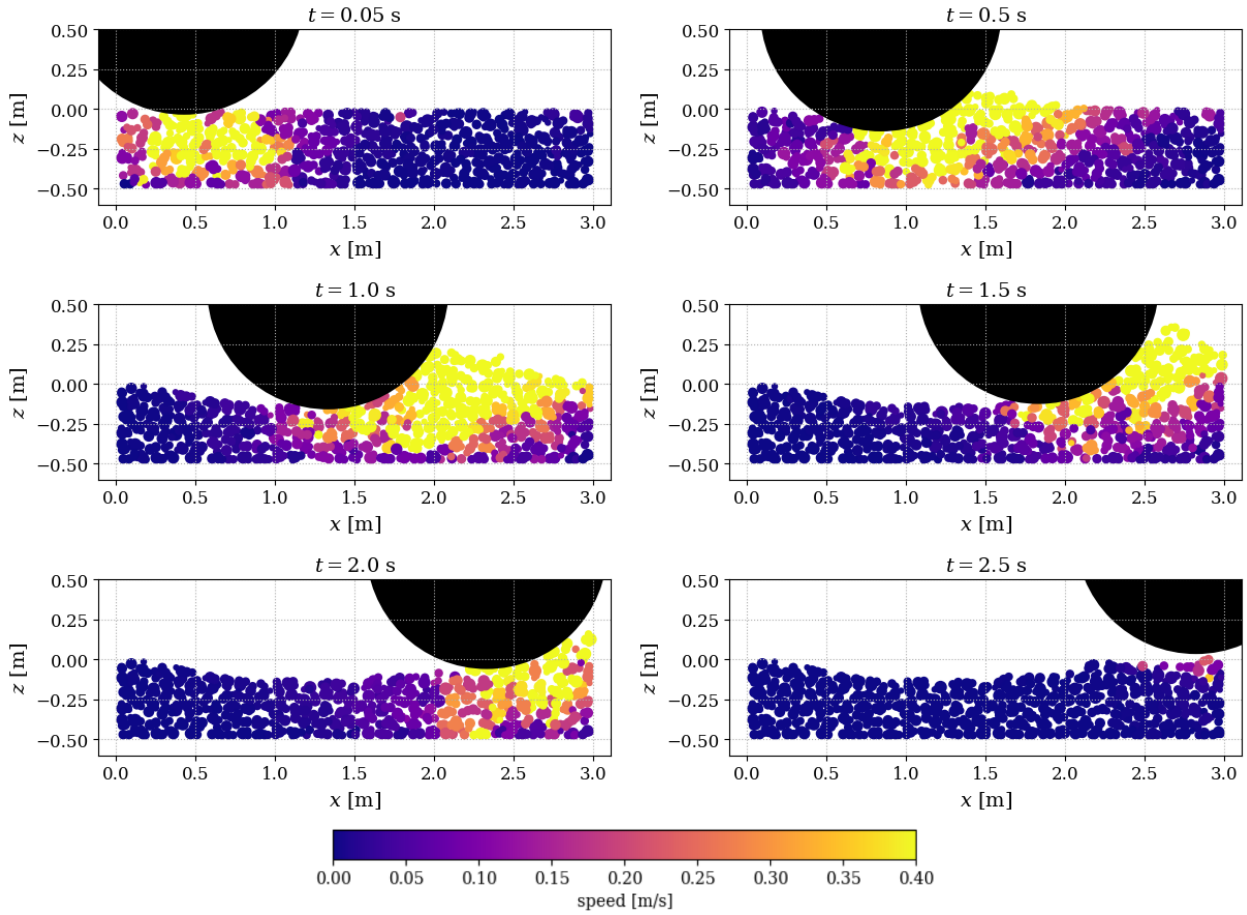

Figure 7.4: *Velocity magnitude of particles in the centre of a bed with $E = 10$ GPa during compaction. After initial placement, the drum starts vibrating and rolling over the bed.*

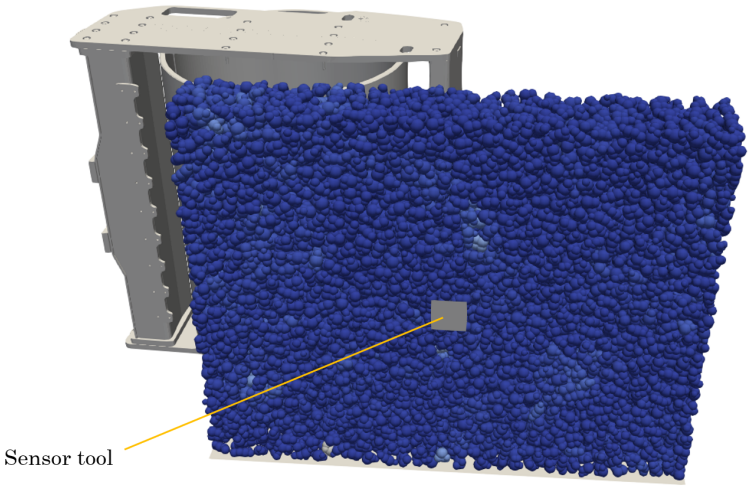

Figure 7.5: *Placement of the sensor tool below the bed. Its area is equal to that of the load cells used in experiments. Contact forces on the tool are used to measure the bed stress at a given depth.*

Table 7.3: Stresses measured at the sensor tool (Figure 7.5). The time passed between the first and last occurrence of a stress spike above half the maximal stress is a measure on the width of the stress curve. Setting $E = 1$ GPa gives good agreement with experiments.

E [GPa]	n_{sph}	fraction [mm]	depth [mm]	max stress [kPa]	time above $0.5 \max \sigma$ [s]
1	4	90/90	500	280	0.25
10	4	90/90	500	381	0.57
20	4	90/90	500	544	0.39
1	4	90/90	1000	121	0.94
20	{4,8}	45/120	500	1047	0.15
20	10	90/90	500	677	0.36
(experiment)		8/90	500	245	0.5
(experiment)		8/90	1000	152	1.5

then decrease in height. This data can be used to measure the width and height of the affected zone. The magnitude of the largest spikes is of interest, as is the time during which vibrations are particularly strong. Table 7.3 shows the maximal measured stress, and the time passed between the first and last occurrence of a spike above half the maximal stress.

As expected, the affected zone appears to be wider at a deeper level, as indicated by the longer time of elevated vibrations at 1000 mm depth. On the other hand, stresses are larger closer to the roller. The magnitude of stresses is therefore necessarily affected by the roller depth, since a roller that sinks deeper into the bed will be closer to the sensor. This is evident in the results when comparing to bed average height from Table 7.2, and it is one cause of the very large stresses observed for the 45/120 material. The depth effect notwithstanding, stiffer material clearly leads to larger bed stresses. This is likely because the roller impact force is larger against a stiff bed.

Comparison with experimental values in Table 7.3 shows that a Young's modulus of 1 GPa appears to capture the stress behaviour well. The corresponding sensor stresses are shown in Figure 7.6. For comparison, the stresses measured at 0.5 m and 1 m depth for the 8/90 material in the experiments are also shown. The general stress behaviour is captured, with the same frequency and an amplitude that is close to experimental results. Judging from the tails of the curves, in the experiments, vibrations are higher when the drum is distant from the load cell. This indicates that the spread of vibrations in the bed is not entirely captured. There is also a small difference in the vertical offset. This could be due to calibration of the experiment equipment. One indication of this is given by comparison with a simple hydrostatic estimate of the pressure at 0.5 and 1 m. The simulation results lie closer to this estimate than the experimental results do. Removing this offset would increase agreement of results further.

7.4 Drum response to impact

The position and velocity of the drum is recorded during simulation. This allows for study of the drum vibratory characteristics, in particular of the acceleration and the spectrum of acceleration frequencies. Compaction theory (Chapter 2) shows that, as the bed gets stiffer, drum oscillations become less harmonic, and behaviours such as double jump and rocking appear. The loads on the drum are also studied.

Drum loads are highly dependent on the bed properties. Figure 7.7 shows the vertical component of the contact force between the bed and the drum for a soft and a stiff material. On a soft bed, the drum remains in continuous contact with the particles and the force oscillates fairly harmonically with the excitation frequency of 29 Hz. On a stiff bed, the impact forces are larger, and the drum lifts off the bed. The contact force alternates between high and low peaks. A study of the drum movement confirms that this is because the drum alternates between low and high lift-offs, also known as double jumps in compaction theory. The same behaviour is observed throughout the simulations, but the ratio between high and low peaks varies. This corresponds clearly to the behaviour predicted in section 2.1. The bed depth does not appear to have a large influence on the contact force. The force is slightly larger for the wider particle fraction bed than for the uniform distribution.

Just as in Intelligent compaction, Fourier analysis is performed on the vertical component of the drum acceleration to derive a measure of the bed stiffness. The frequency spectrum obtained is shown in Figure 7.8 for two 90/90 beds of 4-clumps with $E = 1$ GPa and $E = 20$ GPa. The drum oscillations on the soft bed are harmonic, with the spectrum concentrated at the excitation frequency. For stiffer particles, there are also peaks

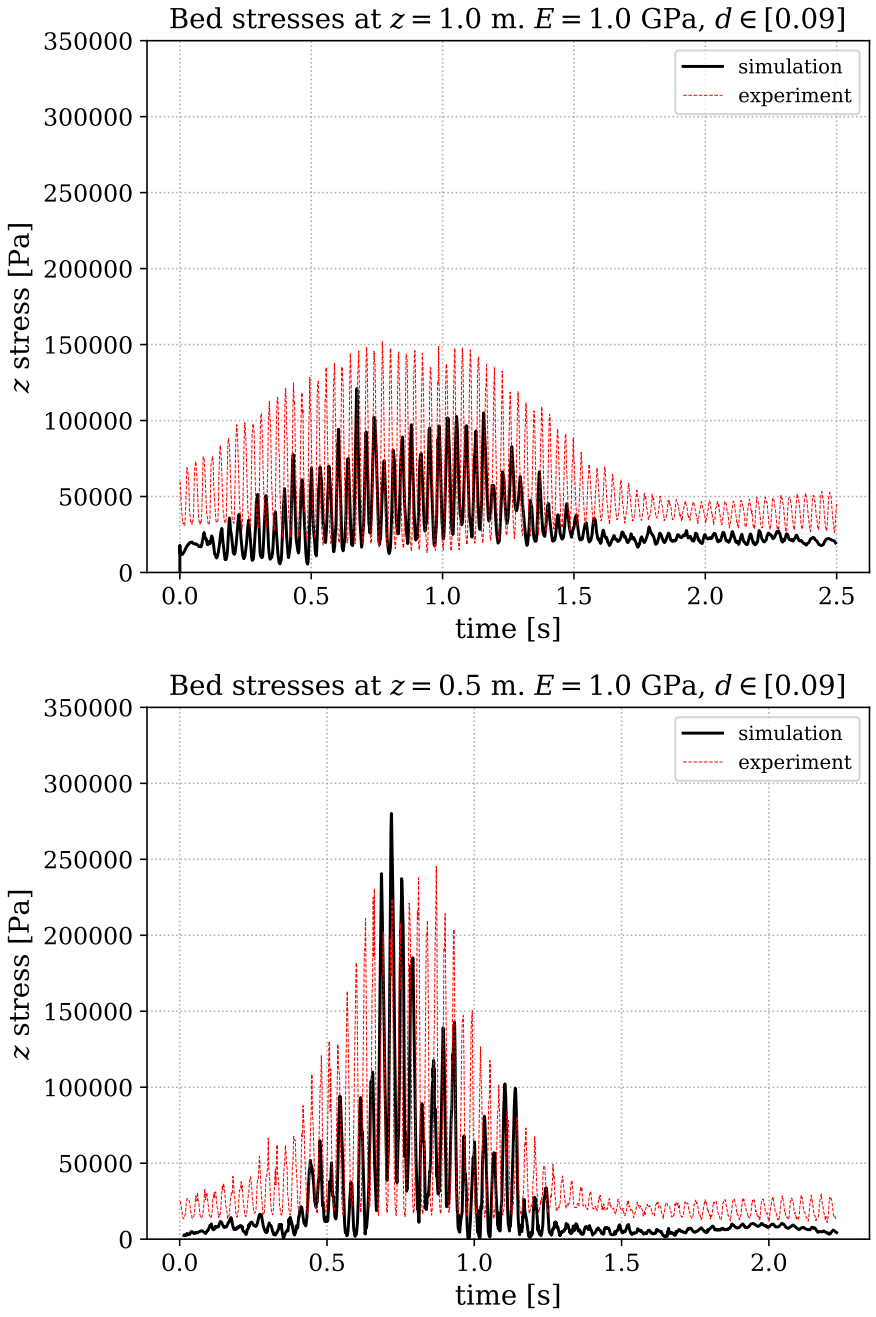

Figure 7.6: *Simulated sensor stresses for 90/90 beds with $E = 1$ GPa at depths 1 m (top) and 0.5 m (bottom). Results measured in experiments are shown in red for comparison.*

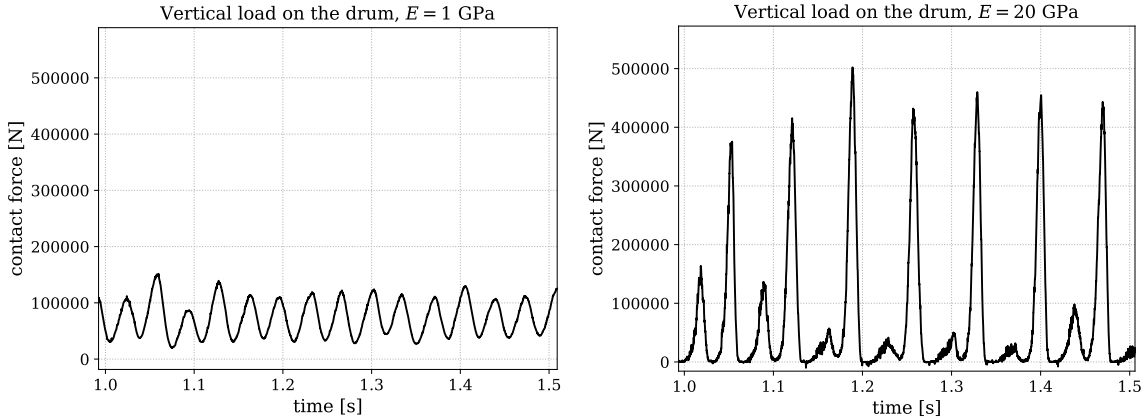

Figure 7.7: *Impact force between the drum and the bed for material with $E = 1$ GPa (left) and $E = 20$ GPa (right). A stiffer material reacts with a larger force on the drum, and the nature of the contact changes. For the soft bed, contact is continuous. In the stiff case, the contact force reaches zero as the drum lifts off. The impacts alternate between high and low, an indication that the drum performs double jumps. This is in accordance with compaction theory (cf. Figure 2.2).*

Table 7.4: Computed CCV values, and the ratio of acceleration amplitudes, corresponding to CMV. This ratio increases with the Young's modulus of the material. CMV and CCV correlate to a large extent.

E [GPa]	n_{sph}	fraction [mm]	depth [mm]	A_{2f}/A_f	CCV
1	4	90/90	500	0.00249	1.3 %
10	4	90/90	500	0.123	40 %
20	4	90/90	500	0.197	62 %
1	4	90/90	1000	0.00352	1.8 %
20	{4,8}	45/120	500	0.199	60 %
20	10	90/90	500	0.183	62 %

of deteriorating magnitude for multiples of the excitation frequency at $1.5f$, $2f$, $2.5f$, and $3f$, as well as a peak at $0.5f$. This behaviour again corresponds to compaction theory.

Table 7.4 shows computed CCV (Equation 2.2), and the ratio of the amplitudes at $2f$ and f, as obtained from Fourier analysis of the acceleration spectrum. This ratio corresponds to the compaction meter value except for a calibration constant (Equation 2.1), and therefore gives a machine measure of the bed stiffness. Both values vary with E, but appear to be unaffected by bed depth and particle fraction.

Finally, one simulation with a timestep of 5×10^{-7}, instead of the 3×10^{-6} used above, shows an increase in the height change from 47.7 mm to 84.4 mm, with a density ratio of 0.967 down from 0.982. The maximum sensor stress does not change by much, decreasing from 280 to 260 kPa. The drum response remains virtually unaltered, with identical CMV (0.00156) and CCV (1.3 %). This means either that results have not yet converged with regard to the timestep, or, perhaps more likely, that there is a variance in the bed response.

7.5 Discussion of results and model limitations

Beds of varying Young's modulus, depth and particle fraction are compacted in the simulations. The resulting bulk density, height change, sensor stresses, and drum movement are analysed. In comparison with experiments and theory, simulations qualitatively capture the drum behaviour to a large extent. Some quantitative agreement with measured bed stresses has also been achieved, but only when keeping the Young's modulus lower than typical values for granite. No significant increase in bulk density of the bed is achieved. Instead, the drum sinks into the bed to a varying degree, due to insufficient shear resistance. Overall, the multibody part of simulation results are more realistic than the DEM part.

The insufficient shear resistance is believed to be caused by a particle shape discretisation that is too coarse,

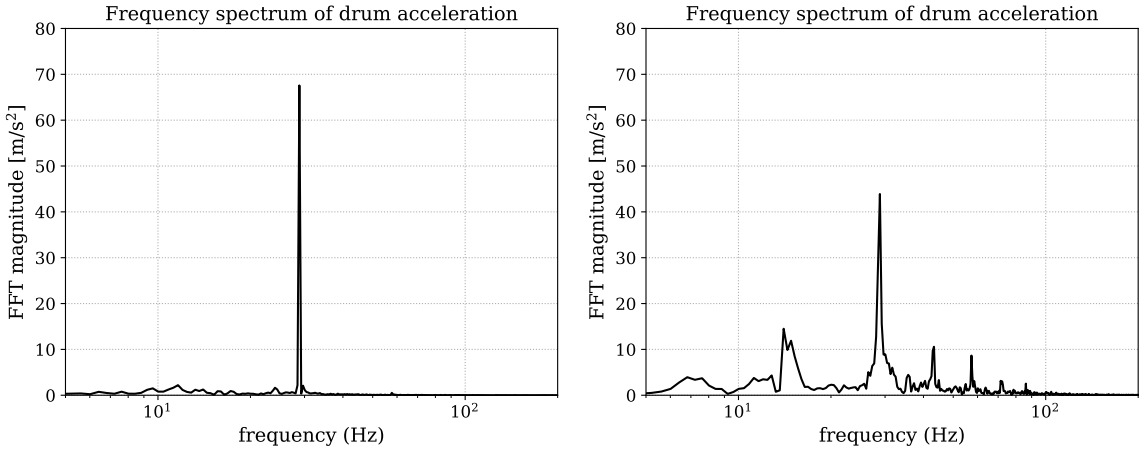

Figure 7.8: *Results of a discrete Fourier analysis of the vertical drum acceleration during compaction of material with different Young's modulus. Left:* $E = 1$ *GPa, right:* $E = 20$ *GPa. On a soft material, the oscillation of the drum is almost entirely harmonic at the excitation frequency 29 Hz. On the stiffer bed, there are also clear subharmonic frequencies at* $0.5f$, $1.5f$, *and* $2f$. *These results are in line with theory, cf. Figure 2.2*

and possibly a simulated particle fraction that is too narrow. Both these problems stem from simplifications made to alleviate the computational effort. Clumps with more subspheres should increase interlocking and friction between particles, giving a more realistic bulk behaviour. Another approach would be to use polyhedral particles rather than clumps. With regard to the particle size, the practical experience is that material of broader fractions is stiffer and denser. However, this is not observed when broadening the fraction from monodisperse 90 mm to the range 45/120 mm. It is possible that an even wider fraction would be stiffer and denser, and that 45/120 is an insufficiently narrow range for small particles to fit between large ones. However, any reduction of the smallest particles is very computationally expensive, since the number of particles grows rapidly and the timestep must be reduced for smaller subsphere radii.

A monodisperse 90 mm bed is very different from the 8/90 bed used in the experiment. There are geometrical limitations in the largest possible bulk density achievable by reconfiguration of monodisperse particles. Simulation of the monodisperse bed therefore cannot be expected to capture the compaction behaviour of broader particle fractions; indeed, an experiment on a monodisperse bed would likely not lead to much compaction either. In reality, the large interparticular forces would lead to abrasion and crushing of the material. Therefore, the machine response simulation results should be more valid than the achieved compaction results. The density reduction of the 45/120 material is more surprising, but it could be because of suboptimal machine vibratory settings. Given that the compaction meter value is high from the start, it seems the drum forces are too high to properly compact the bed, and instead the contact skeleton is smashed. Particles start moving and the bed gets looser. This is in fact precisely what happens in reality, when material is compacted with too much vibratory force. On the other hand, 20 GPa is a realistic value for granite. It is possible that a lower Young's modulus or a reduced vibratory frequency would achieve a denser bed. However, any optimisation of machine parameters lies outside the scope of this text.

8 Conclusions

The scope of this thesis is relatively wide. The studied literature covers compaction theory, DEM models and methods, multibody dynamics, DEM-MBS coupling, calibration, and elementary rock mechanics. A multibody dynamics solver is developed, as well as software for coupling the two solvers. The roller front module mechanical system is analysed and a representative multibody model is established. All implementation is verified, and a limited parameter study is carried out in an attempt to calibrate the DEM model. The project also includes participation in a few days' experimental work on compaction. Finally, all parts are combined, which enables simulation of compaction on a high degree of complexity, compared to the methods widely used in previous literature. The necessity of all parts included in the final simulations is what motivates the wide scope.

Given these results, the objectives of the thesis have been reached. The implementation of a multibody solver, machine model, DEM ground model, and co-simulation framework has been verified. The bed stiffness in the simulations can be estimated via the ratio of acceleration amplitudes, as is done in reality during Intelligent compaction. Contact forces are measured, as well as the stress at the bottom of the bed. The achieved compaction and the relation to particle size distribution and bed depth are investigated to an extent. The machine behaviour is recorded for different particle material parameters, and found to mimic continuous compaction and double jump as known from theory.

There are two main limitations: the minimum particle size and the particle discretisation. Both limitations are to an extent related to computational cost. A comparison of 90/90 and 45/120 materials shows that reducing the minimum particle diameter by half increased the computation time by a factor of four. Further stretching of the lower limit has not been feasible, even though the tested particle size range is far too narrow for the results to be representative of the experiment. The second limitation relates to the particle shape. It can be assumed that an increase in the number of subspheres in clumps would improve results; there is such an indication in the compaction simulations. But the calibration also pinpoints another problem: the shape of the stress-strain curve is different in experiments and simulations. Also, parameter variation seemingly only has a marginal effect on the behaviour. These two facts indicate that the applied model is not entirely valid for compaction. This could be due to the clump representation, or the contact force model.

Further work should first focus on assessing the effects of the delimitations drawn in this thesis. For example, a more complete parameter calibration including a convergence assessment and a statistical study is likely necessary to confidently capture the bed response to compaction. As another example, a study of the variance between bed realisations should be performed to assert the reliability of the results. On the other hand, in this work, implementation is prioritised over full validation of simulations, and the end result of this thesis should be seen in the light of what new simulations it enables, rather than the results of the simulations that have been carried out.

Overall, this thesis has demonstrated the feasibility of a coupled MBS-DEM method for compaction simulation, and presented all steps up to a working full-scale implementation. In addition, the advantages and limitations of the method have been highlighted. This provides a good basis for continued work on coupled compaction simulations. However, as is shown in the calibration step, adjustment of the DEM particle and contact force models is needed to capture compaction behaviour and hysteresis. A possible candidate for such an attempt is to use polyhedral particles. Regarding the particle size distribution, one longer compaction simulation with a wider fraction should be run, to further assess the effect of size range on the compaction effect. Finally, all simulations for this work were run on CPUs. A GPU version of the multisphere Demify code is currently under development, and use of a state-of-the-art GPU solver is expected to improve computational capacity by at least two orders of magnitude. This will likely widen the future range of applicability of coupled compaction simulation.

References

[1] I. S. Tyuremnov and A. S. Morev. "New Criterion for Continuous Compaction Control Systems by Soil Vibratory Rollers". *Proceedings of the 5th International Conference on Industrial Engineering (ICIE 2019)*. Ed. by A. A. Radionov et al. Cham: Springer International Publishing, 2020, pp. 585–593. ISBN: 978-3-030-22063-1. DOI: 10.1007/978-3-030-22063-1_62.

[2] X. Zhu et al. Assessment of compaction quality of multi-layer pavement structure based on intelligent compaction technology. *Construction and Building Materials* **161** (Feb. 2018), 316–329. DOI: 10.1016/j.conbuildmat.2017.11.139. URL: https://doi.org/10.1016/j.conbuildmat.2017.11.139.

[3] *Pavement Structure*. 2020. URL: https://pavementinteractive.org/reference-desk/design/structural-design/pavement-structure/.

[4] *TRVK Väg - Trafikverkets tekniska krav Vägkonstruktion*. CE certificate. Borlänge: Trafikverket/Swedish Transport Administration, 2011.

[5] F. Hellman. *Packning av obundet material i vägkonstruktioner*. Publication. VTI, 2011.

[6] J.-L. Briaud and D. Saez. "Recent Developments in Soil Compaction". *Ground Improvement Case Histories*. Elsevier, 2015, pp. 275–308. DOI: 10.1016/b978-0-08-100698-6.00009-x.

[7] Z. An et al. Dynamic optimization of compaction process for rockfill materials. *Automation in Construction* **110** (2020), 103038. DOI: 10.1016/j.autcon.2019.103038.

[8] P. A. Cundall and O. D. L. Strack. A discrete numerical model for granular assemblies. *Géotechnique* **29**.1 (1979), 47–65. DOI: 10.1680/geot.1979.29.1.47. eprint: https://doi.org/10.1680/geot.1979.29.1.47. URL: https://doi.org/10.1680/geot.1979.29.1.47.

[9] D. Liu et al. Process Simulation and Mesoscopic Analysis of Rockfill Dam Compaction Using Discrete Element Method. *International Journal of Geomechanics* **20**.6 (June 2020), 04020047. DOI: 10.1061/(asce)gm.1943-5622.0001679. URL: https://doi.org/10.1061/(asce)gm.1943-5622.0001679.

[10] K. Wu et al. Discrete Element Modeling of Vibration Compaction Effect of the Vibratory Roller in Roundtrips on Gravels. *Journal of Testing and Evaluation* **49**.5 (May 2020), 20190910. DOI: 10.1520/jte20190910. URL: https://doi.org/10.1520/jte20190910.

[11] X. Zhao. Parameters Selection of Asphalt Pavement Compaction Based on Virtual Experiment. *Applied Mechanics and Materials* **361-363** (2013), 1584–1589. DOI: 10.4028/www.scientific.net/amm.361-363.1584.

[12] T. Pei and X. Yang. Compaction-induced stress in geosynthetic-reinforced granular base course – A discrete element model. *Journal of Rock Mechanics and Geotechnical Engineering* **10**.4 (2018), 669–677. DOI: 10.1016/j.jrmge.2018.02.005. URL: https://doi.org/10.1016/j.jrmge.2018.02.005.

[13] Z. Zhao et al. Control method of seedbed compactness based on fragment soil compaction dynamic characteristics. *Soil and Tillage Research* **198** (2020), 104551. DOI: 10.1016/j.still.2019.104551.

[14] J. Quist. *Ansökan Stödbidrag – Undersökning av separationseffekter vid kompaktering av obundna material, Beviljat projekt 13820*. SBUF - Svenska Byggbranschens Utvecklingsfond. 2020.

[15] Y. G. Popov and E. K. Chabutkin. "Increasing Efficiency of Vibratory Rollers Through Adjusting Magnitude of Disturbing Force". *Lecture Notes in Mechanical Engineering*. Springer International Publishing, Nov. 2019, pp. 567–576. DOI: 10.1007/978-3-030-22063-1_60. URL: https://doi.org/10.1007/978-3-030-22063-1_60.

[16] R. Anderegg and K. Kaufmann. Intelligent Compaction with Vibratory Rollers: Feedback Control Systems in Automatic Compaction and Compaction Control. *Transportation Research Record: Journal of the Transportation Research Board* **1868**.1 (Jan. 2004), 124–134. DOI: 10.3141/1868-13. URL: https://doi.org/10.3141/1868-13.

[17] K. Kim and S. Chun. Finite element analysis to simulate the effect of impact rollers for estimating the influence depth of soil compaction. *KSCE Journal of Civil Engineering* **20**.7 (2016), 2692–2701. DOI: 10.1007/s12205-016-0013-8.

[18] V. N. Tarasov et al. Methods of the analytical study of vibratory drum forced vibrations during the soil compaction. *Journal of Physics: Conference Series* **1441** (Jan. 2020), 012117. DOI: 10.1088/1742-6596/1441/1/012117. URL: https://doi.org/10.1088/1742-6596/1441/1/012117.

[19] H. Thurner and Å. Sandström. "A new device for instant compaction control". *Proceedings of International Conference on Compaction*. Vol. II. Paris, 1980, pp. 611–614.

[20] J. A. Scherocman, S. Rakowski, and K. Uchiyama. "Intelligent Compaction, Does It Exist?" *Proceedings of the Fifty-Second Annual Conference of the Canadian Technical Asphalt Association (CTAA)*. Canadian Technical Asphalt Association. Laval, Quebec, Canada: Polyscience Publications, Nov. 2007, pp. 373–398.
[21] D. Pietzsch and W. Poppy. Simulation of Soil Compaction with Vibratory Rollers. *Journal of Terramechanics* **29**.6 (1992), 585–597.
[22] A. Kordestani. "Ride Vibration and Compaction Dynamics of Vibratory Soil Compactors". PhD thesis. Concordia University, Apr. 2010. DOI: 10.13140/RG.2.1.2818.9685.
[23] S. A. Imran et al. Modeling the Dynamics of Asphalt–Roller Interaction during Compaction. *Journal of Construction Engineering and Management* **143**.7 (2017), 04017015. DOI: 10.1061/(asce)co.1943-7862.0001293.
[24] J. Pan and A. Selby. Simulation of dynamic compaction of loose granular soils. *Advances in Engineering Software* **33**.7-10 (2002), 631–640. DOI: 10.1016/s0965-9978(02)00067-4. URL: https://doi.org/10.1016/s0965-9978(02)00067-4.
[25] B. Kenneally et al. Finite element analysis of vibratory roller response on layered soil systems. *Computers and Geotechnics* **67** (2015), 73–82. DOI: 10.1016/j.compgeo.2015.02.015.
[26] S. Ghorbani. "Simulation of soil-to-tool interaction using Discrete Element Method (DEM) and Multibody Dynamics (MBD) coupling". MA thesis. Iowa State University, 2019.
[27] S. A. Ghoohaki. "High-fidelity modeling of a backhoe digging operation using an explicit multibody dynamics finite element code with integrated discrete element method". MA thesis. Purdue University, 2013.
[28] A. G. Sane. "High-fidelity modelling of a bulldozer using an explicit multibody dynamics finite element code with integrated discrete element method". MA thesis. Purdue University, 2015.
[29] A. Roy. "Experimental validation of non-cohesive soil using discrete element method". MA thesis. Purdue University, 2018.
[30] G. K. Barrios and L. M. Tavares. A preliminary model of high pressure roll grinding using the discrete element method and multi-body dynamics coupling. *International Journal of Mineral Processing* **156** (2016), 32–42. DOI: 10.1016/j.minpro.2016.06.009.
[31] A. A. Shabana. *Dynamics of multibody systems*. Cambridge University Press, 2009. DOI: 10.1017/cbo9781107337213. URL: https://doi.org/10.1017/cbo9781107337213.
[32] E. Stoneking. "Newton-Euler Dynamic Equations of Motion for a Multi-Body Spacecraft". *AIAA Guidance, Navigation and Control Conference and Exhibit*. American Institute of Aeronautics and Astronautics, Aug. 2007. DOI: 10.2514/6.2007-6441. URL: https://doi.org/10.2514/6.2007-6441.
[33] D. Chappuis. *Constraints Derivation for Rigid Body Simulation in 3D*. 2013. URL: https://danielchappuis.ch/download/ConstraintsDerivationRigidBody3D.pdf.
[34] B. Graf. *Quaternions and dynamics*. 2008. eprint: arXiv:0811.2889.
[35] M. Neto and J. Ambrósio. Stabilization Methods for the Integration of DAE in the Presence of Redundant Constraints. *Multibody System Dynamics* **10** (Aug. 2003), 81–105. DOI: 10.1023/A:1024567523268.
[36] *Dynapac CA3500D Single drum vibratory rollers: Product information*. 2020. URL: https://dynapac.com/en/products/compaction/dynapac-ca3500d.
[37] *CA3500 Spare parts list Vibratory roller*. Nov. 2018.
[38] *CA2500/2800/3500/4000 - Operation & Maintenance manual*. Nov. 2019. URL: https://dynapac.com/en/products/compaction/dynapac-ca3500d.
[39] W. C. Swope et al. A computer simulation method for the calculation of equilibrium constants for the formation of physical clusters of molecules: Application to small water clusters. *The Journal of Chemical Physics* **76**.1 (Jan. 1982), 637–649. DOI: 10.1063/1.442716. URL: https://doi.org/10.1063/1.442716.
[40] C. Thornton, S. J. Cummins, and P. W. Cleary. An investigation of the comparative behaviour of alternative contact force models during elastic collisions. *Powder Technology* **210**.3 (2011), 189–197. DOI: 10.1016/j.powtec.2011.01.013.
[41] M. Lu and G. R. McDowell. The importance of modelling ballast particle shape in the discrete element method. *Granular Matter* **9**.1-2 (July 2006), 69–80. DOI: 10.1007/s10035-006-0021-3. URL: https://doi.org/10.1007/s10035-006-0021-3.
[42] H. Kruggel-Emden et al. A study on the validity of the multi-sphere Discrete Element Method. *Powder Technology* **188**.2 (Dec. 2008), 153–165. DOI: 10.1016/j.powtec.2008.04.037. URL: https://doi.org/10.1016/j.powtec.2008.04.037.
[43] *Ballast för obundna och hydrauliskt bundna material till väg- och anläggningsbyggande*. CE certificate. Stockholm: Skanska Industrial Solutions AB, Nov. 2018.

[44] J. F. Peters et al. Large-Scale Discrete-Element Modeling for Engineering Analysis: Case Study for the Mobility Cone Penetrometer. *Journal of Geotechnical and Geoenvironmental Engineering* **145**.12 (Dec. 2019), 04019111. DOI: 10.1061/(asce)gt.1943-5606.0002174. URL: https://doi.org/10.1061/(asce)gt.1943-5606.0002174.

[45] M. Stahl and H. Konietzky. Discrete element simulation of ballast and gravel under special consideration of grain-shape, grain-size and relative density. *Granular Matter* **13**.4 (Dec. 2010), 417–428. DOI: 10.1007/s10035-010-0239-y. URL: https://doi.org/10.1007/s10035-010-0239-y.

[46] S. Lommen, G. Lodewijks, and D. L. Schott. Co-simulation framework of discrete element method and multibody dynamics models. *Engineering Computations* **35**.3 (2018), 1481–1499. DOI: 10.1108/ec-07-2017-0246.

[47] J. Quist. "DEM Modelling and Simulation of Cone Crushers and High Pressure Grinding Rolls". PhD thesis. Gothenburg: CHALMERS UNIVERSITY OF TECHNOLOGY, 2017. ISBN: 978-91-7597-544-3.

[48] C. J. Coetzee. Calibration of the discrete element method and the effect of particle shape. *Powder Technology* **297** (2016), 50–70.

[49] H. Q. Do, A. M. Aragón, and D. L. Schott. A calibration framework for discrete element model parameters using genetic algorithms. *Advanced Powder Technology* **29** (2018), 1393–1403.

[50] M. Rackl and K. J. Hanley. A methodical calibration procedure for discrete element models. *Powder Technology* **307** (2017), 73–83.

[51] S. MotahariTabari and I. Shooshpasha. Evaluation of coarse-grained mechanical properties using small direct shear test. *International Journal of Geotechnical Engineering* (Aug. 2018), 1–13. DOI: 10.1080/19386362.2018.1505310. URL: https://doi.org/10.1080/19386362.2018.1505310.

[52] E. Arpaz. Determination of restitution coefficients for various granite samples. *Arabian Journal of Geosciences* **8**.7 (Aug. 2014), 5285–5294. DOI: 10.1007/s12517-014-1571-z. URL: https://doi.org/10.1007/s12517-014-1571-z.

[53] *Young's Moduli of Rock Types*. 2020. URL: http://community.dur.ac.uk/~des0www4/cal/dams/geol/mod.htm.

[54] B. Vásárhelyi. A possible method for estimating the Poisson's rate values of the rock masses. *Acta Geodaetica et Geophysica Hungarica* **44**.3 (Sept. 2009), 313–322. DOI: 10.1556/ageod.44.2009.3.4. URL: https://doi.org/10.1556/ageod.44.2009.3.4.

DEPARTMENT OF MECHANICS AND MARITIME SCIENCES
DIVISION OF VEHICLE ENGINEERING AND AUTONOMOUS SYSTEMS
CHALMERS UNIVERSITY OF TECHNOLOGY
Gothenburg, Sweden
www.chalmers.se

CHALMERS
UNIVERSITY OF TECHNOLOGY